Journal of Volcanology and Geothermal Research 192 (2010) 69–84

Contents lists available at ScienceDirect

Journal of Volcanology and Geothermal Research

journal homepage: www.elsevier.com/locate/jvolgeores

Linking experimental and natural vesicle textures in Vesuvius 79AD white pumice

Thomas Shea [a,*], Lucia Gurioli [b,c,d], Jessica F. Larsen [e], Bruce F. Houghton [a], Julia E. Hammer [a], Katharine V. Cashman [f]

[a] Department of Geology and Geophysics, SOEST, University of Hawaii, 96822, Honolulu, HI, United States
[b] Clermont Université, Université Blaise Pascal, Laboratoire Magmas et Volcans, BP 10448, F-63000 Clermont-Ferrand, France
[c] CNRS, UMR 6524, LMV, F-63038 Clermont-Ferrand, France
[d] IRD, R 163, LMV, F-63038 Clermont-Ferrand, France
[e] Geophysical Institute, University of Alaska Fairbanks, 99775, Fairbanks, AK, United States
[f] Department of Geological Sciences, University of Oregon, 97403, Eugene, OR, United States

ARTICLE INFO

Article history:
Received 16 July 2009
Accepted 16 February 2010
Available online 3 March 2010

Keywords:
vesicles
phonolite
Vesuvius
textural characterization
decompression experiments
size distribution
magma ascent rate

ABSTRACT

Vesicle populations in volcanic pumice provide a partial record of shallow magma ascent and degassing. Here we compare pumice textures from the well-characterized 79AD Vesuvius eruption to those generated during isothermal decompression experiments. Three series of experiments were conducted using starting material from the first two phases of the eruption (eruptive units EU1 and EU2). Samples were decompressed from 100 or 150 MPa to final pressures of 10–25 MPa using conditions appropriate for simulating eruption conditions ($T = 850$ °C, $dP/dT = 0.25$ MPa/s). The experiments differed not only in starting material but also in temperature at which samples were annealed prior to decompression, which determined the initial number of crystals present in the melt. Results show that experiments approach the vesicle number densities and sizes of pumice samples, but show narrower size distributions. The wider size range of pumice samples suggests continuous, rather than instantaneous nucleation, which may reflect non-linear rates of decompression. All experiments exhibited equilibrium degassing, a process that was probably aided by heterogeneous bubble nucleation on oxide microlites. We conclude that delayed bubble nucleation cannot explain the explosivity of the Vesuvius eruption, which instead appears to require high rates of magma decompression.

1. Introduction

Vesicles in volcanic rocks provide valuable information on the processes occurring in magma conduits and storage systems (e.g. Cashman and Mangan, 1994). Three complementary approaches provide constraints on vesiculation in magmas: textural measurements, laboratory experiments, and physical/numerical models. Textural measurements of vesicle size, number and spatial distribution in natural samples are used to infer the processes responsible for their formation (e.g., Klug and Cashman, 1994; Klug et al., 2002; Polacci et al., 2003; Gurioli et al., 2005; Sable et al., 2006; Adams et al., 2006, Lautze and Houghton, 2007; Polacci et al., 2007). Although natural tephra samples are the best available "tracers" of vesiculation in any eruption, they represent a frozen textural state, which might have been acquired prior to, during, and after magmatic fragmentation. Decompression experiments document processes of bubble nucleation, growth, coalescence, and collapse that may occur during magma ascent, although the small volumes of material used often prevent scaling of vesicle size, number and porosity to natural systems. Models of bubble nucleation and growth link experiments to conduit processes, and ultimately, shed light on conditions required to produce violent explosive eruptions (Toramaru, 1989; Toramaru, 1995; Lyakhovsky et al., 1996; Jaupart, 1996; Vergniolle, 1996; Lovejoy et al., 2004; Mangan et al., 2004; Massol and Koyaguchi, 2005; Yamada et al., 2005; Toramaru, 2006; Gonnermann and Manga, 2007).

Of the three approaches described above, laboratory experiments provide a critical link between field observations and modeling through quantification of kinetic parameters such as bubble nucleation and growth rates, volatile solubility, diffusivity, and surface tension. Most experimental vesiculation studies have examined rhyolitic magmas (Hurwitz and Navon, 1994; Lyakhovsky et al., 1996; Gardner et al., 1999; Mourtada-Bonnefoi and Laporte, 1999; Mangan and Sisson, 2000; Gardner et al., 2000; Larsen and Gardner, 2000; Mourtada-Bonnefoi and Laporte, 2002; Martel and Schmidt, 2003; Mourtada-Bonnefoi and Laporte, 2004; Larsen et al., 2004; Lensky et al., 2004; Burgisser and Gardner, 2005; Gardner, 2007; Cluzel et al., 2008) because they produce the most violent eruptions, and their high viscosity precludes problems associated with rapid microlite crystallization and bubble-melt decoupling in laboratory capsules. Sparser experimental data exist on lower viscosity melts such as basalts (Bai et al., 2008), dacites (Mangan et al., 2004; Suzuki et al., 2007) and phonolites (Larsen and Gardner, 2004;

* Corresponding author. Tel.: +1 808 956 8558.
E-mail address: tshea@hawaii.edu (T. Shea).

0377-0273/$ – see front matter © 2010 Elsevier B.V. All rights reserved.
doi:10.1016/j.jvolgeores.2010.02.013

Larsen et al., 2004; Iacono Marziano et al., 2007; Larsen, 2008; Mongrain et al., 2008).

Here, we examine the decompression and vesiculation of phonolites at conditions relevant to the 79AD eruption of Vesuvius, and compare experimental textures to those of pumice deposited during the opening and first Plinian phases of the eruption. Both natural and experimental data are then compared to models of bubble formation to determine (1) limiting conditions of equilibrium H_2O exsolution, (2) the correspondence between number densities, modal vesicle size, and size distribution of pumice and experimental samples, and (3) the influence of microlites on nucleation. We find that 79AD K-phonolites nucleate heterogeneously on microlites, exsolve efficiently even at low temperatures, and produce number densities close to those measured in natural samples. On the other hand, bubble size distribution comparisons between experimental and natural samples suggest that natural ascent processes are probably more complex than what has been tested to date in the laboratory environment. We suggest that the most viable way to mimic natural bubble size populations through experiments is to apply non-linear decompression pathways, possibly resulting in multiple nucleation and growth pulses.

2. The 79AD eruption of Vesuvius

Nearly 2000 years ago, Vesuvius volcano produced one of the largest and deadliest historical eruptions, burying the Roman towns of Herculaneum, Pompeii, Oplontis and Stabiae under meters of both fallout tephra and pyroclastic density current (PDC) deposits (e.g. Lirer et al., 1973; Sigurdsson et al., 1982, 1985; Cioni et al., 1992). The eruption (volcanic explosivity index VEI = 6, Cioni et al., 2008) lasted over 20 h and produced a total of 2–3 km^3 of deposits, calculated as dense rock equivalent (DRE). Pumice composition and color varied from a white phonolitic to a gray tephri-phonolitic composition during the course of the eruption, which is thought to reflect pre-eruptive zoning of the magma reservoir (Sigurdsson et al., 1990; Cioni et al., 1995). According to this model, the magma that produced white pumice (hereafter referred to as "white" magma) was an un-erupted remnant from the ~3900 BP eruption of Avellino, which had differentiated and cooled to ~850 °C (Cioni, 2000) over about 2000 years (Lirer et al., 1973, Cioni et al., 1995). During the 79AD eruption, batches of hotter tephritic magma intruded the storage region, heated the lower portion of the white magma to ≤925 °C (Shea et al., 2009) and mixed with white magma to produce the tephri-phonolite, which produced the later gray pumice deposits.

Herein, we focus on the white magma and, more specifically, on the opening sub-Plinian (EU1) and Plinian (EU2) stages. Our objective is to characterize vesiculation processes from the onset to the sustained plinian phase of the eruption. The opening phase (EU1) formed a ~15 km-high buoyant column that was advected eastward by lower tropospheric winds (Sigurdsson et al., 1985) and deposited fine-grained pumice tens of kilometers from the vent (Fig. 1a and b). The unit varies from 0 to 15 cm in thickness (Fig. 1c) and blankets the flanks of the volcano. After a small column collapse event generated a poorly dispersed PDC (EU1pf, Cioni et al., 2000), the sustained activity increased in intensity and a much higher ~25–30 km plume formed (Fig. 1b), was carried south-east by stratospheric winds (Rolandi et al., 2008), and deposited EU2 pumice hundreds of kilometers from the eruptive center (Sigurdsson et al., 1985). EU2 is ≤140 cm thick at the base of Vesuvius (Cioni et al., 1992), thins outward and then thickens again (>100 cm) towards the Sorrento peninsula (Sigurdsson et al., 1985; Fig. 1a, c).

3. Background: textural investigation of products from the 79AD eruption and vesiculation experiments in phonolites

The products of the 79AD eruption of Vesuvius have been characterized by Gurioli et al. (2005), who examined textural evidence for the origin of changes in eruptive behavior during two important transitions (i.e. white to gray pumice EU2–EU3 and sustained plinian activity to caldera collapse EU3–EU4) using vesicle and crystal textures. We focus on conditions related to the onset of eruptive activity (EU1) and subsequent transition to the first Plinian phase (EU2). In particular, we used decompression experiments to explore the effects of varying starting conditions (composition and microlite content) on conditions of vesicuation and, by

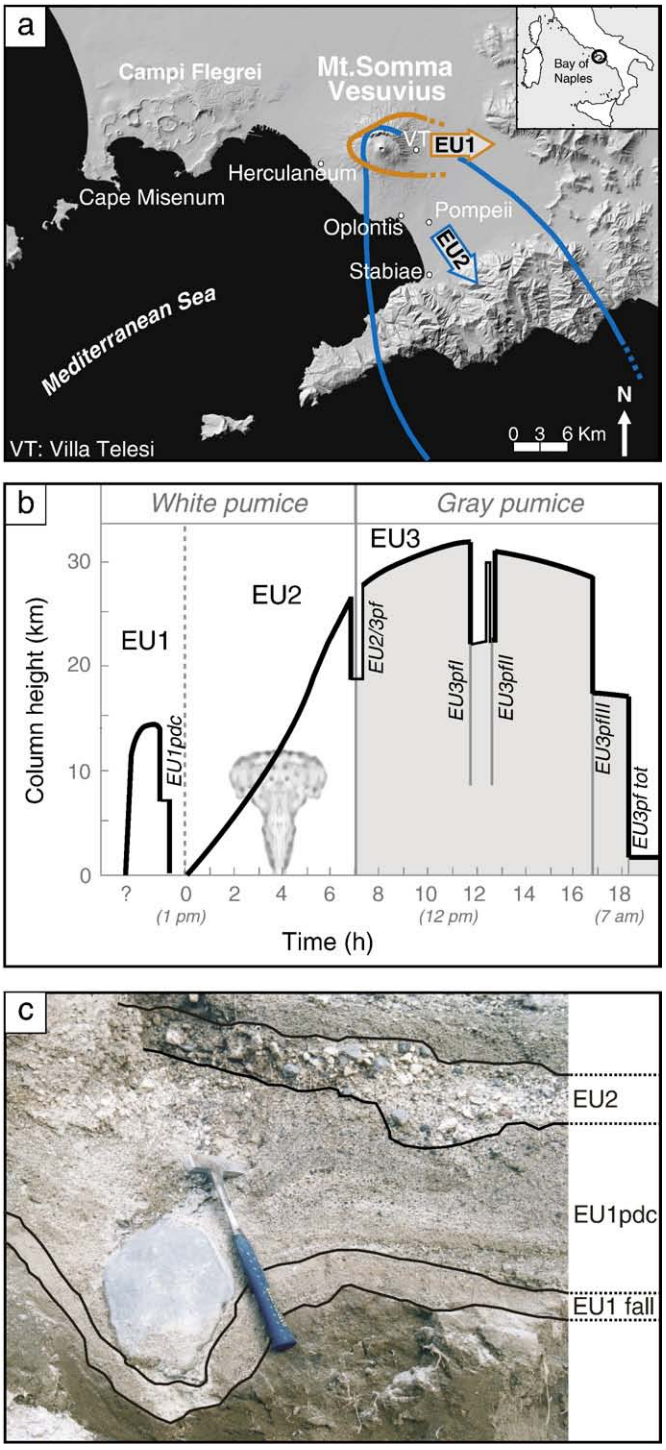

Fig. 1. (a) DEM of the Bay of Naples and the region surrounding Mt. Vesuvius in Italy, overlain by 10 cm-isopachs of fallout deposits ejected during both the opening (EU1) and early Plinian (EU2) phases of the 79AD eruption. Note how the dispersion is much more reduced for EU1. Pumice samples from EU1 and EU2 used in this study were collected at Villa Telesi and Pompeii, respectively. (b) Interpretative plot of eruptive column height in function of time through the eruption, along with the approximate timing of various fallout and pyroclastic density current events (modified from Carey and Sigurdsson, 1987). (c) Outcrop showing EU1 and EU2 separated by a pyroclastic density current deposit (EU1pdc). Hammer for scale.

inference, on the course of the eruption. Textural data for EU2 is presented in Gurioli et al. (2005); textural data for EU1 is presented here.

Previous decompression experiments that use Vesuvius phonolite starting compositions have explored conditions that allow equilibrium degassing to be maintained. Iacono Marziano et al. (2007) used superliquidus melts (1050 °C) to determine limiting decompression rates of ≥1.7 MPa/s for homogeneous nucleation, and ≤0.0028 MPa/s to maintain near-equilibrium conditions of degassing. Larsen (2008) started experiments at subliquidus temperatures (900 and 950 °C) where bubble nucleation appeared heterogeneous even at high decompression rates (3–17 MPa/s), requiring $\Delta P \leq 50$ MPa to trigger vesiculation. These experiments indicated, however, a big contrast in the degassing behavior between the higher temperature experiments, where equilibrium volatile contents were maintained during decompression, and the lower temperature experiments, where experiments deviate strongly from equilibrium trends. Our experiments extend the range of experimental conditions to lower temperatures (850 °C) and slower decompression (0.25 MPa/s); these conditions lie within the inferred temperature and decompression rate for the early phase of the 79AD eruption, thereby allowing us to link the experiments to the natural environment.

4. Methods

4.1. Decompression experiments

We used multiple-step decompression (MSD) experiments to investigate bubble nucleation and growth in Vesuvius phonolites at conditions relevant to the 79AD eruption. 5 MPa pressure drops were followed by 20-second holding periods to replicate a linear, integrated ascent rate of 10 m/s (0.25 MPa/s), which represents the average ascent velocity derived from the modeling from Papale and Dobran (1993). It is a conservative estimate considering that input rates of 20–40 m/s are required to reproduce the high mass discharge rates calculated for the EU2 phase of the eruption (Carey and Sigurdsson, 1987) in other numerical ascent models (e.g. CONFLOW, Mastin and Ghiorso, 2000). Although magma ascent during eruption is non-linear (e.g. Neri et al., 2002), the use of a linear decompression rate of 0.25 MPa/s was most practical in the laboratory environment.

4.2. Starting material and experimental setup

Starting material for decompression experiments are 2–3 cm-sized EU1 and EU2 pumice clasts (see Fig. 1 for sampling locations) that show minor differences in composition (Table 1), with slightly lower SiO_2, FeO, MgO, and CaO and higher Al_2O3, Na_2O, and K_2O in EU1 compared to EU2. Two sets of experiments using powdered pumices from EU1 and EU2 were placed at the initial pressure ($P_I = 150$ MPa) and temperature ($T = 850$ °C) for 5–7 days under water-saturated conditions ($a_{H_2O} = 1$) inside Au, Ag, or Ag-Pd capsules loaded into Rene-style Waspaloy vessels pressurized with H_2O. This step ensured that the material would reach near-equilibrium starting conditions, and that pore space was minimized (Larsen and Gardner, 2004; Larsen, 2008). A series of MSD with initial pressure $P_I = 100$ MPa and temperature $T = 850$ °C from prior experiments (Larsen, unpublished data) was also available to compare with series at $P_I = 150$ MPa. Those MSD experiments underwent an additional annealing step at 1000 °C prior to re-equilibration at 850 °C that initially served to eliminate most microlites that might modify nucleation behavior, thus allowing us to assess the effect of crystal content. Hereafter, the 150 MPa series for EU1 and EU2 are labeled "series A and B" respectively, and the annealed 100 MPa series available for EU2 is labeled "series C". Oxygen fugacity (fO_2) was maintained at Ni–NiO ± 0.5 to 1 log unit (Rutherford, 1996; Scaillet and Pichavant, 2004) in saturation experiments by inserting nickel filler rods into the vessels. Capsules were placed on a hot plate at 150 °C and weighed before and after each saturation run to ensure that no water had been lost. Splits of resulting glass slabs were then reloaded into several capsules 30 mm in length and 4 mm in diameter, each crimped and welded. Each capsule was then placed into rapid quench-capable cold-seal vessels at $T = 850$ °C, $P_I = 150$ MPa for 1–2 h, then decompressed stepwise and quenched at ending pressures (P_F) between 125

Table 1
Chemical analyses of EU1 and EU2 samples.

wt.%	EU1 14-1	EU2 V15-2-9
SiO_2	54.91 (0.26)	55.41 (0.38)
TiO_2	0.31 (0.14)	0.26 (0.11)
Al_2O_3	22.30 (0.23)	21.97 (0.45)
FeO*	2.16 (0.13)	2.90 (0.38)
MnO	0.24 (0.08)	0.24 (0.12)
MgO	0.23 (0.03)	0.65 (0.07)
CaO	3.11 (0.22)	3.69 (0.25)
Na_2O	6.22 (0.19)	5.32 (0.21)
K_2O	9.89 (0.42)	9.17 (0.39)
Cl[a]	0.54 (0.08)	0.26 (0.14)
P_2O_5	0.09 (0.04)	0.12 (0.05)
Totals[b]	99.20 (0.41)	99.76 (0.58)
n[c]	14	19

[a] Cl is reported as oxide weight percent.
[b] Original totals with analyses normalized to 100%.
[c] Total number of electron microprobe analyses of glass created by melting powders in $Au_{75}Pd_{25}$ tubing for 10 min at 1300 °C.

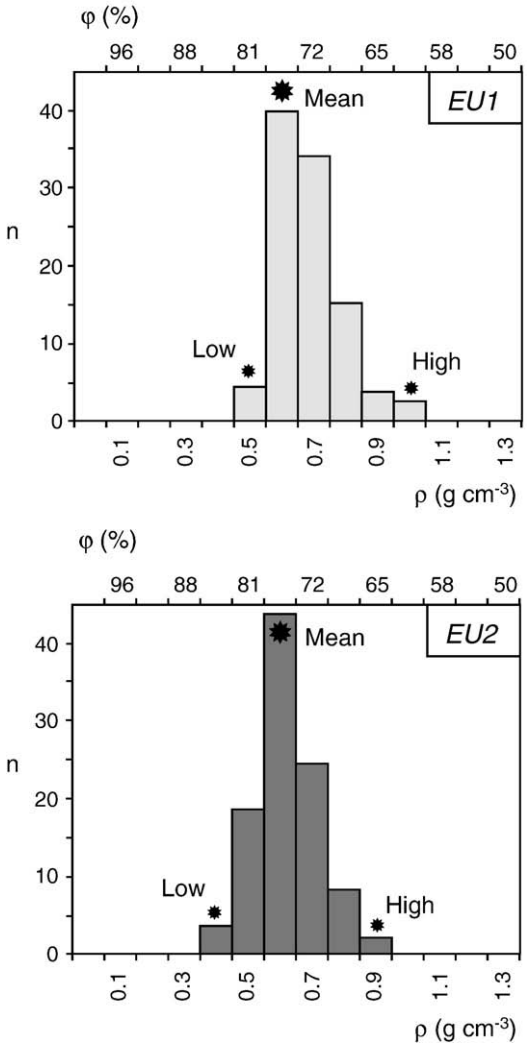

Fig. 2. Density variations within pumice clasts sampled from EU1 (above) and EU2 (below, modified from Gurioli et al., 2005). For each, three representative samples (low, mean and high densities) were chosen at strategic locations within the distribution. Corresponding vesicularities are also reported on top of each plot. n = number of clasts.

Table 2
Summary of textural measurements performed in Natural and Experimental samples.

	P_i[a]	P_F[b]	ΔP[c]	t[d]	ϕ_{2D}[e]	ϕ_{3D}[f]	$\phi_{L<0.01}$[g]	L_{mean}[h]	$L_{maj\text{-}mode}$[i]	$L_{min\text{-}mode}$[j]	N_V[k]	N_{Vcorr}[l]	D. type[m]	N_{Vox}[n]	J[o]	G_{mode}[p]
Natural samples																
$EU1_{low}$	–	–	–	–	73.8	81.4	2.9	0.27	0.03	0.381	0.63×10^6	3.4×10^6	*p* (3.42)	–	–	–
$EU2_{low}$	–	–	–	–	82.1	83.4	7.3	0.289	0.019	2.403	1.4×10^6	8.7×10^6	*p* (3.44)	–	–	–
$EU1_{mean}$	–	–	–	–	64.7	75	2.8	0.099	0.076	–	0.64×10^6	2.6×10^6	*p* (3.39)	–	–	–
$EU2_{mean}$	–	–	–	–	67.5	77	8.1	0.171	0.038	3.026	2.5×10^6	11×10^6	*p* (3.50)	–	–	–
$EU1_{high}$	–	–	–	–	51.1	62.1	7.9	0.108	0.048	0.604	2.9×10^6	7.8×10^6	*p* (3.47)	–	–	–
$EU2_{high}$	–	–	–	–	61.9	70.9	12.1	0.087	0.015	1.517	3.5×10^6	12×10^6	*p* (3.63)	–	–	–
Series A																
1-2a	150	125	25	100	3.8	8.3	3.48	0.009	0.005	–	0.75×10^6	0.82×10^6	*e*/*p*	9×10^6	8.21×10^3	5.10×10^{-5}
1-2b	150	100	50	200	6.3	12.1	5.12	0.017	0.013	–	0.95×10^6	1.1×10^6	*e* (376)	16×10^6	1.31×10^3	7.49×10^{-5}
1-2c	150	75	75	300	11.8	19.9	4.15	0.031	0.05	–	0.64×10^6	0.8×10^6	*p* (2.42)	11×10^6	0	37.53×10^{-5}
1-2d	150	50	100	400	23.2	35	2.82	0.09	0.158	–	0.22×10^6	0.34×10^6	e (187)	–	0	107.48×10^{-5}
1-2e	150	25	125	500	49.5	63	0.56	0.154	0.25	–	0.08×10^6	0.23×10^6	e (63)	–	0	92.19×10^{-5}
Series B																
2-3a	150	125	25	100	1.7	5.2	2.54	0.002	0.006	–	3.4×10^6	3.6×10^6	*e* (752)	44×10^6	36.2×10^3	6.31×10^{-5}
2-3b	150	100	50	200	5.6	11	10.18	0.006	0.008	–	5.2×10^6	5.9×10^6	*e* (712)	52×10^6	51.1×10^3	1.63×10^{-5}
2-3c	150	75	75	300	15.5	25.1	7.48	0.028	0.02	–	7.4×10^6	9.9×10^6	*e* (164)	45×10^6	11.2×10^3	12.01×10^{-5}
2-3d	150	50	100	400	22.4	33.9	8.73	0.035	0.05	–	4.5×10^6	6.8×10^6	*p* (2.51)	–	0	30.17×10^{-5}
2-3e	150	25	125	500	43.4	57.3	7.88	0.053	0.079	–	3.7×10^6	8.6×10^6	*e* (143)	–	0	29.48×10^{-5}
Series C																
26a	100	75	25	100	4.9	10	3.02		0.016	–	0.23×10^6	0.26×10^6	*e* (245)	3.3×10^6	2.56×10^3	15.76×10^{-5}
26b	100	50	50	200	16.3	26.1	3.14	0.038	0.05	–	0.27×10^6	0.36×10^6	*e* (144)	3.4×10^6	0.54×10^3	34.08×10^{-5}
26c	100	25	75	300	45.1	59	0.23	0.07	0.079	–	0.07×10^6	0.17×10^6	*e* (64)	–	0	29.15×10^{-5}
26d	100	10	90	360	76.5	82	0.05	0.193	0.252	–	0.01×10^6	0.08×10^6	*e* (22)	–	0	288.00×10^{-5}

[a] Starting experimental pressure (MPa).
[b] Final quench pressure (MPa).
[c] Total decompression (MPa).
[d] Total decompression time (s).
[e] 2D-vesicularity obtained by area measurements (%).
[f] 3D-vesicularity obtained by density-derived measurements (%).
[g] Vesicularity for vesicle populations with diameters <0.01 mm (%).
[h] Mean vesicle diameter (mm).
[i] Major mode of size distribution (mm).
[j] Minor mode of size distribution (mm).
[k] Vesicle number density (mm^{-3}).
[l] Vesicle number density corrected for vesicularity (mm^{-3}).
[m] Type of distribution: *p*: power-law distribution of form $N_V(>L)\sim f(L^{-d})$ with corresponding exponents *d* in parentheses. *e*: exponential distribution of form $N_V\sim f(e^{-aL})$ with corresponding exponents *a* in parentheses. *e*/*p*: undetermined, both show good fit. All exponents have been derived from $\log(N_V>L)$ vs. $\log(L)$ plots. Best-fit functions have a minimum of $R^2>0.94$.
[n] Oxide microlite number density corrected for vesicularity (mm^{-3}).
[o] Nucleation rates ($mm^{-3}\ s^{-1}$).
[p] Growth rates calculated using modal sizes ($mm\ s^{-1}$).

and 25 MPa. In general, decompression to lower pressures resulted in foam collapse or fragmentation although one successful run at $P_F = 10$ MPa was integrated into the experimental dataset.

4.3. Experimental conditions

The experimental temperature of 850 °C is within the range determined for the 79AD magmas from prior studies (Barberi et al., 1981; Cioni et al., 1995) and at the lower bound of the 850–925 °C found by Cioni et al. (1998) and Shea et al. (2009). Storage pressures have been constrained at 100–150 MPa by Cioni (2000) on the basis of volatiles in melt inclusions although Iacono Marziano et al. (2007)and Scaillet et al. (2008) have inferred pressures of 200 MPa using phase equilibria and water solubility experiments, respectively. We used $P_i = 150$ MPa for both EU1 and EU2 runs. Finally, although CO_2 might have been present during earlier stages of magma storage (Scaillet and Pichavant, 2004), absence of CO_2 within melt inclusions indicates that the magma was H_2O-saturated ($H_2O \leq 6.5$ wt.%) immediately prior to ascent (Cioni, 2000). Water-saturation was consequently assumed for all decompression experiments.

4.4. Textural characterization

Measurements of sample vesicularity, vesicle size distribution (VSD), vesicle volume distribution (VVD), and number density per unit volume melt (N_{Vcorr}) were obtained using methods described in Shea et al. (2010). Sample vesicularity is determined by measuring sample weight in air and water, assuming a fixed solid fraction density (Houghton and Wilson, 1989). Density/vesicularity histograms were used to select three samples representative of the low, mean and high density end-members for further textural characterization (Fig. 2). While density measurements are easily achievable for cm-sized pumice clasts, they are not feasible for experimental samples that have volumes of a few cubic mm. Thus, experimentalists often choose to consider the 2D vesicularity as representative of the 3D vesicularity (e.g. Gardner et al., 1999; Gardner et al., 2000; Martel and Schmidt, 2003; Mangan et al., 2004; Mourtada-Bonnefoi and Laporte, 2004; Burgisser and Gardner, 2005; Cluzel et al., 2008), or derive vesicularity using stereological corrections methods (e.g. Mourtada-Bonnefoi and Laporte, 2004; Larsen and Gardner, 2004). In an attempt to estimate how 2D (i.e. "image vesicularity",ϕ_{2D}) compares to true

Fig. 3. SEM images of EU1 and EU2 natural pumice samples. (a) low, (c) mean and (e) high density clasts chosen within EU1, and (b) low, (d) mean, (f) and high density clasts from EU2. Walls are somewhat thicker in EU1 and the high density end-member (e) possesses different textural zones. (g) and (h) are close-ups of mean density clasts from EU1 and EU2 respectively. Note in (h) the slightly higher proportion of very small bubbles in between glass nodes compared to (g).

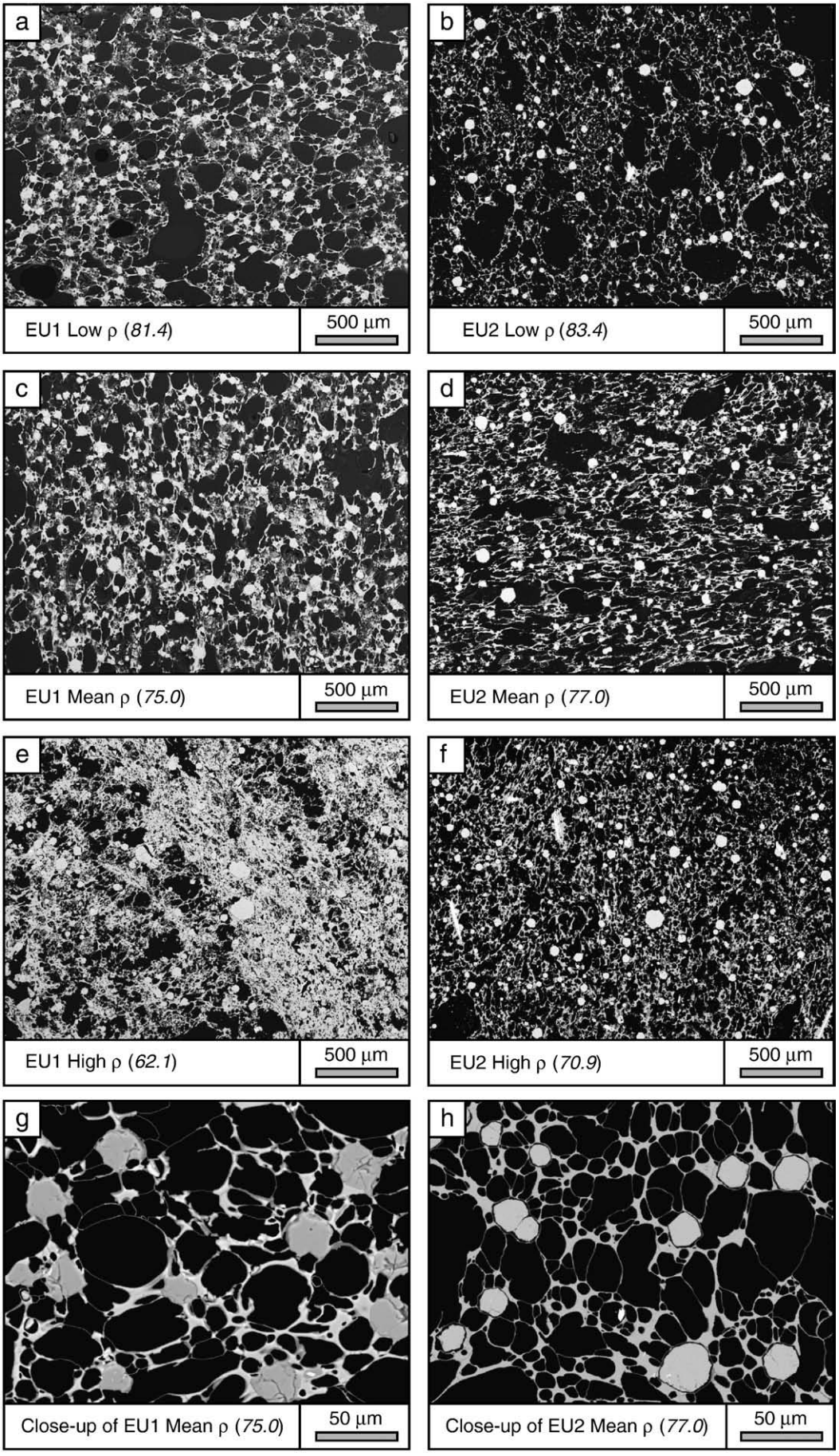
a
EU1 Low ρ (81.4)
500 μm
b
EU2 Low ρ (83.4)
500 μm
c
EU1 Mean ρ (75.0)
500 μm
d
EU2 Mean ρ (77.0)
500 μm
e
EU1 High ρ (62.1)
500 μm
f
EU2 High ρ (70.9)
500 μm
g
Close-up of EU1 Mean ρ (75.0)
50 μm
h
Close-up of EU2 Mean ρ (77.0)
50 μm

vesicularity ("density-derived vesicularity", ϕ_{3D}), we gathered data from 5 explosive and 1 effusive eruptions, and derived a best-fit equation (see Appendix A for a full description):

$$\phi_{3D} = -6.762 \times 10^{-2}\phi_{2D}^2 + 1.5574\phi_{2D} + 2.5 \quad (1)$$

VSDs, VVDs and N_Vs were derived via a Matlab®-based algorithm (cf. FOAMS, Shea et al., 2010) based on formulations by Sahagian and Proussevitch (1998). Vesicle number densities were corrected for calculated vesicularities (N_{Vcorr}, Table 2) to provide information on the number of bubbles that nucleated and survived coalescence and collapse. Finally, to test the influence of microlites on vesiculation, oxide number densities N_{Vox} per unit volume were also measured within decompression experiments.

5. Results

5.1. Textural characterization of Vesuvius 79AD white pumice

Detailed descriptions of EU2 textures can be found in Gurioli et al. (2005), and new measurements concern EU1 only. Nonetheless, to facilitate comparison, both EU1 and EU2 textural features are summarized in the following paragraphs.

5.1.1. Observations

Textural measurements for both EU1 and EU2 are reported for clasts that represent the mode and extremes of the density distribution for each deposit (e.g., Shea et al., 2010). Progressing from low to higher densities (Fig. 3a, c, d and b, d, f), large (>0.5 mm) vesicles become sparser and glass walls thicken. In all samples, larger vesicles have complex shapes while smaller ones (i.e. <0.1 mm) are round. Vesicle walls are smooth, and bubbles are either located away from large crystals or arranged as intricate radial webs around leucites (Fig. 3g and h). Tiny ~1–3 μm oxide microlites (dominantly titanomagnetite) are abundant and homogeneously distributed within the glass of all natural samples. While the low and mean density end-members in both EU1 and EU2 display similar textures and vesicularities, EU1 high density clasts are less vesicular (~62% for EU1 high and 71% for EU2 high) because of alternating dense and vesicular regions (Fig. 3e) that may be associated with shear-bands. In contrast, the high density end-member of EU2 (Fig. 3f) is relatively homogeneous. EU2 also contains more minute (i.e. <0.01 mm) vesicles than EU1 (e.g. compare Fig. 3g with h). Neither EU1 nor EU2 show evidence of post-fragmentation expansion (e.g., bread-crusting, differential bubble expansion, Polacci et al., 2001; Klug et al., 2002), which may affect the interpretation of measurements. Throughout this contribution, we therefore assume that the textures by EU1 and EU2 pumices are frozen records acquired during or prior to fragmentation.

5.1.2. Measurements

Measurements of natural and experimental vesicle sizes, numbers, and other relevant parameters are reported in Table 2. Vesicularities for the two sets of natural samples are 62, 75, 81% low, mean and high densities respectively for EU1, and 71, 77, 83% for EU2 (Fig. 2). Vesicle size distributions (VSD, Fig. 4a) differ in that the mean sample of EU1 lacks the larger portion of the population visible in the EU2 mean. Both EU1 and EU2 low density clasts show extended tails towards large vesicles (>1.5 mm) while the high density end-members contain only vesicles <1.5 mm. VSD curves, which are used to infer the steadiness of the vesiculation process (e.g. Cashman and Marsh, 1988; Mangan and Cashman, 1996, Klug et al., 2002; Adams et al., 2006), show gradual rather than abrupt changes. Kinks within the larger populations (>500 μm) are artifacts of lower sampling frequency associated with geometric binning.

Size distributions expressed as volume fraction histograms (vesicle volume distributions "VVD", Fig. 4b) provide a more detailed view of the larger (and less numerous) vesicles. Low density clasts have a dominant mode at 20–30 μm, and a secondary mode at larger sizes caused by coalescence (e.g. Klug et al., 2002). EU1 and EU2 mean density clasts show minor differences at comparable vesicularities (75 and 77% EU1 and EU2 respectively); EU1 is unimodal whereas EU2 could be bi-modal. Lastly, EU1 and EU2 high density distributions both have one dominant mode. For high density samples, in contrast with low and mean density pumices, vesicularities strongly differ (62% and 71% for EU1 and EU2 respectively) probably due to shearing-induced bubble collapse within narrows zones of EU1 (Fig. 3e). In general, dominant modes are about two to three times larger in size in EU1 compared to EU2 (Table 2), irrespective of clast vesicularity. Calculated N_{Vcorr} are systematically higher in EU2 than in EU1 for all clast densities (close to 3×10^6 mm^{-3} for EU1 and around 1×10^7 mm^{-3} for EU2). The smallest vesicles (L<0.01 mm) are the most numerous (VSDs, Fig. 4a) and their contribution to total porosity is non-negligible (~3 to 12% vesicularity $\phi_{L<0.01}$, Table 2).

Gurioli et al. (2005) interpreted EU2 to have undergone continuous nucleation and growth. Additional information is provided by its comparison with EU1 data; EU1 vesicle modes (0.03, 0.08, and 0.05 mm, cf. Table 2) are slightly larger than EU2 (0.02, 0.04, and 0.015 mm), which could indicate more time in the conduit after nucleation of late-stage bubble populations or simply differing ascent rates in the upper regions of the conduit prior to fragmentation. In all pumice samples analyzed, cumulative VSDs are best characterized by power-law distributions (cf. Blower et al., 2001) with exponents d>3 (Table 2).

5.2. Textural characterization of laboratory experiments

To provide direct comparison between natural samples and experiments, observations of the development of vesicle textures during decompression are followed by descriptions of textural measurements made within each experimental series.

5.2.1. Bubble vesiculation during experiments–observations

The evolution of the exsolution process in series A and B (P_I = 150 MPa) and C (P_I = 100 MPa) is illustrated in Fig. 5 by SEM photos of experimental charges (see Table 2 for measurements). Bubbles nucleate soon after decompression (Fig. 5a, b, c), indicating that a large supersaturation is not required to initiate vesiculation in H_2O-saturated Vesuvius phonolites. As expected, bubbles grow larger at lower ending pressures and start to coalesce at the lowest pressure reached (P_F = 25 MPa in series A and B, and P_F = 10 MPa for series C).

At P_F = 125 MPa, the numerous small bubbles present within series A and B experiments appear homogeneously distributed within the melt (Fig. 5a and b), often associated with oxides (titanomagnetite and ± hematite, Fig. 5d, e, f). At P_F = 50 MPa, vesicles have grown much larger, although EU2 samples retain smaller bubbles. After decompression of P_F = 25 MPa, series A is dominated by closely-spaced large bubbles separated by thin walls, whereas series B contains fewer but larger bubbles separated by thick glass walls. Coalescence areas appear more dominant within series B. At the lowest pressure tested, series A and B have calculated vesicularities of 63 and 57% respectively, which are lower than in most natural 79AD samples, and are likely a consequence of incomplete decompression. The most apparent differences can be expressed in terms of bubble shape and outline: large series A vesicles are mostly round with smooth walls, whereas series B vesicles show irregular shapes with ragged walls. Even at very low ΔP (P_F = 125–100 MPa), tiny series B vesicles show faceted outlines whereas series A vesicles are round (Fig. 5a and b). This striking difference can be attributed to the high numbers of 1–3 μm-sized sanidine microlites within series B glass (Fig. 5e), whereas series A glass lacks any microlites other than oxides (Fig. 5a).

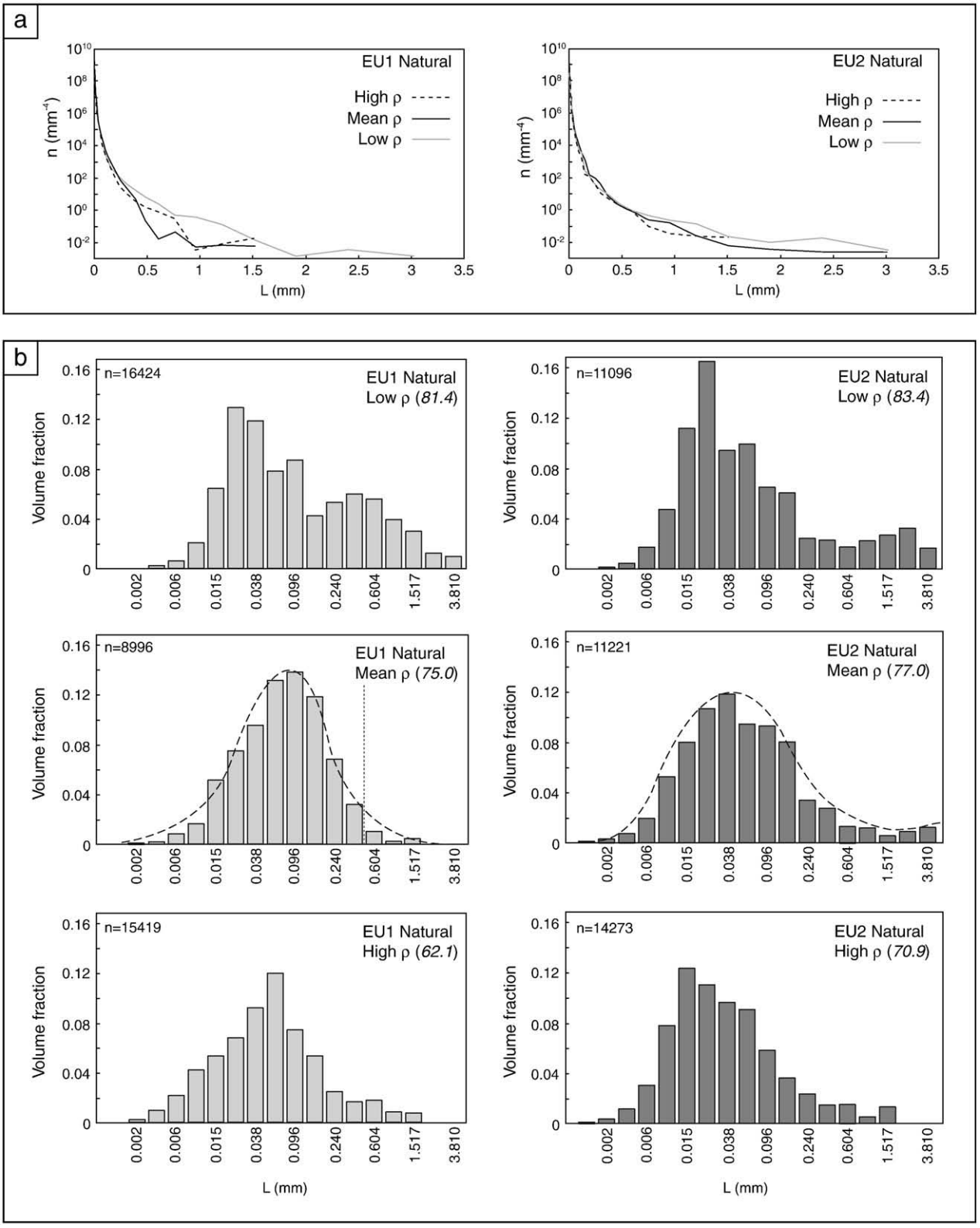

Fig. 4. (a) Vesicle size distributions in terms of number densities for EU1 and EU2 vs. the equivalent diameter (L, linear scale). All three pumice densities considered are reported. (b) Vesicle size distributions in terms of volume fractions vs. equivalent diameter (L, geometric scale) display different modes present within the samples. For more practical viewing of the results, the number of bins has been halved; thus the modes reported in Table 2 do not necessarily correspond to the values displayed here on the x-axis. Note that volume fractions sum to vesicularity values for each sample. n = number of vesicles analyzed.

Series C experiments involved the same EU2 starting material used for Series B experiments, but differ considerably. Much like in series A, vesicles are dominantly round, their boundaries smooth, and the surrounding glass is clear and homogeneous containing fewer oxide microlites (Fig. 5f). At a similar ending pressure of $P_F = 25$ MPa, vesicularity is comparable to series A and B (59%) and at $P_F = 10$ MPa

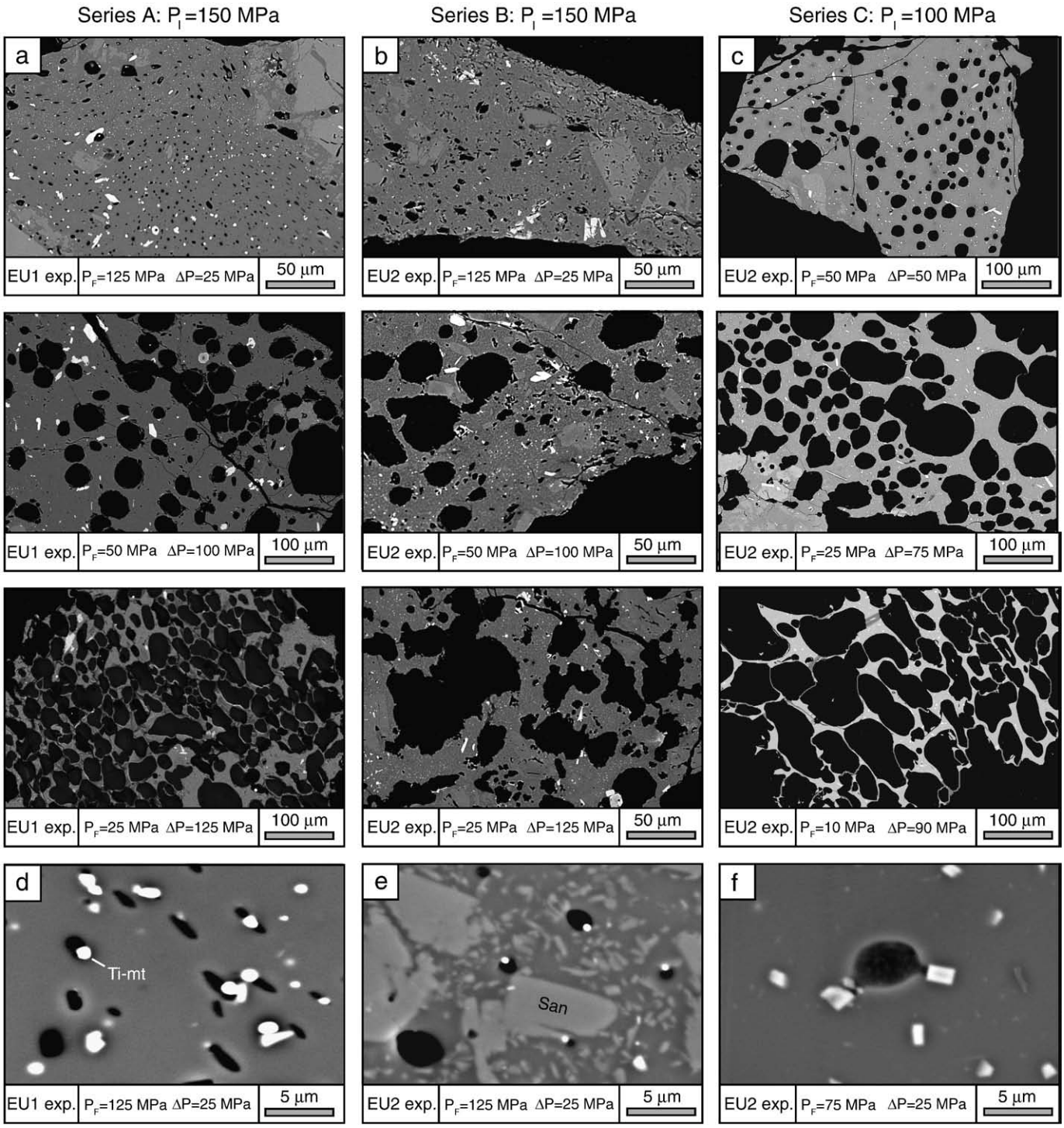

Fig. 5. SEM images of experimental samples quenched at different pressure conditions. (a) Series A and (b) series B started at $P_I = 150$ MPa and quenched at $P_F = 100$, 50 and 25 MPa, and (c) series C started at $P_I = 100$ MPa and quenched at $P_F = 50$, 25 and 10 MPa. Vesicles in series B have fairly distorted shapes and ragged glass walls compared to series A and C or natural samples. (d), (e), and (f) are close-ups (5000X magnification) of groundmasses from all three series showing bubbles often nucleate on titanomagnetites. Note the numerous sanidine microlites within series B compared to series A and C.

attain 82% as vesicle walls become extremely thin (Fig. 5c). Judging from vesicle shape, coalescence appears to be more dominant in series C than in other series: glass walls are often deformed and seem to be on the verge of rupturing (Fig. 5c).

In terms of general appearance, EU1 and EU2 natural samples resemble more with series A and C than Series B. Compared to series A and C, however, vesicle walls are typically thinner in natural samples and glass nodes are less prominent. In addition, the number of small

Fig. 6. Vesicle size distributions measured within experimental samples from series A, B and C at different final pressures. Typically, due to the small sample size, vesicles bigger than 0.240 mm cannot be accounted for. The shaded region represents the portion of the size distribution for which we cannot make inferences. Size distribution curves (dashed lines) for EU1 and EU2 means are reported along with their corresponding series. Note that volume fractions sum to vesicularity values for each sample. n = number of vesicles analyzed.

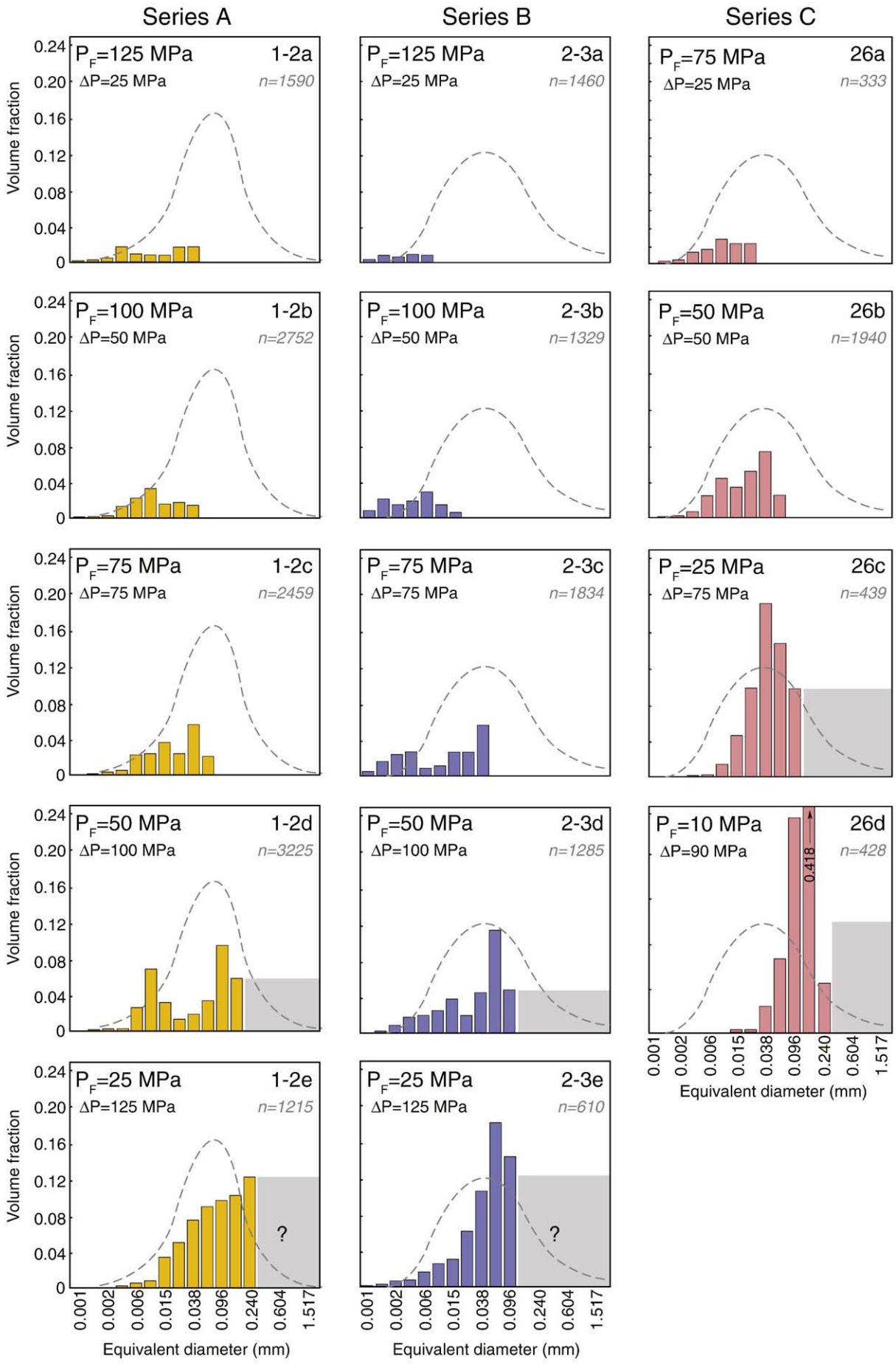
Series A
Series B
Series C
P_F=125 MPa
ΔP=25 MPa
1-2a
n=1590
2-3a
n=1460
26a
n=333
P_F=100 MPa
ΔP=50 MPa
1-2b
n=2752
2-3b
n=1329
P_F=50 MPa
26b
n=1940
P_F=75 MPa
ΔP=75 MPa
1-2c
n=2459
2-3c
n=1834
P_F=25 MPa
26c
n=439
P_F=50 MPa
ΔP=100 MPa
1-2d
n=3225
2-3d
n=1285
P_F=10 MPa
ΔP=90 MPa
26d
n=428
0.418
P_F=25 MPa
ΔP=125 MPa
1-2e
n=1215
2-3e
n=610
?
Volume fraction
0.24
0.20
0.16
0.12
0.08
0.04
0
0.001
0.002
0.006
0.015
0.038
0.096
0.240
0.604
1.517
Equivalent diameter (mm)

vesicles arranged in between large bubbles is much higher in natural samples, where configurations closer to Apollonian packing (i.e., minimization of space by packing spheres of varying radii) are reached. In contrast, experimental samples have a limited size range, even after extensive decompression.

5.2.2. Measurements

Identical quantification procedures to those used for natural samples were employed to characterize decompression experiments. Unfortunately, due to the reduced sample volume within experimental capsules, observations are limited to about 4 mm^2 in area and measurements are restricted to a 0.001–0.240 mm interval. Because modes are not well depicted by VSDs, the distributions are reported only as VVDs (Fig. 6), with EU1 and EU2 mean density distributions shown for comparison. Inspection of the smaller size range (0.001–0.01 mm) reveals that both series A and B possess small vesicles throughout decompression, in contrast with series C, where they disappear with decompression. All three series have dominant modes that increase in size with decompression, but do not achieve the size range seen in pumice samples (Fig. 6). Interestingly, series A and B VVDs are polymodal until $P_F = 25$ MPa, where only one mode remains, although the limited measurable size range may mask secondary modes associated with coalescence. Series C preserves only one mode and has larger modal sizes than Series B.

Vesicle number densities (N_{Vcorr}, Table 2) in all three series show rapid increases before reaching a plateau (series B) or declining (series A and C; Fig. 7). Series A reaches a maximum of $N_{Vcorr} \approx 10^6$ mm^{-3}, which drops to 10^5 mm^{-3} at $\Delta P = 125$ MPa ($P_F = 25$ MPa). In contrast, series B attains values of 10^7 mm^{-3}. Series C N_Vs are significantly lower than series A and B, reaching a maximum of 4×10^5 mm^{-3}. These experimental number densities barely reach the range of N_Vs measured in natural samples, with the exception of series B, where number densities overlap with the most vesicular EU2 sample. Most experimental cumulative VSDs show distributions that follow exponential functions (Table 2) with exponents decreasing with increasing decompression.

6. Discussion

6.1. Assumptions inherent to experimental procedure

Before laboratory experiments can be compared to the natural samples, several underlying assumptions need further consideration. Initial materials used for these experiments were crushed into fine powder and then either annealed at 1000 °C or inserted directly into experimental capsules for equilibration at high pressure and temperature prior to decompression. Using powders without fusing them at high temperatures (i.e. series A and B) presents the disadvantage that pore spaces or hydration bubbles may be present at the onset of decompression (Larsen and Gardner, 2000, 2004). In series A and B samples, a few hydration bubbles can be observed but are in such small numbers that their contribution is considered insignificant (cf., Gardner et al., 1999). In comparison, fusing samples prior to equilibration (i.e. series C) reduces pore spaces, but has the drawback of annealing some microlites that might otherwise be present within the natural melt stored in the crust prior to eruption.

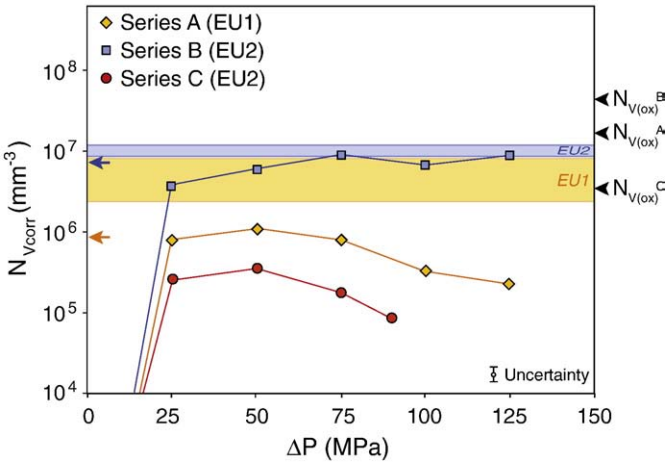

Fig. 7. Vesicle number density (N_{Vcorr}) variations within experiments from all three series in function of the amount of decompression undergone (ΔP). Number density ranges measured in natural pumice from low to high density clasts are also included on the *y*-axis. The maximum uncertainty calculated is reported on the bottom right. The two arrows on the *y*-axis show values taken for calculations leading to Fig. 11 (see text).

6.2. Heterogeneous nucleation in 79AD Vesuvius phonolites

Our experiments show that <25 MPa of decompression was required to initiate vesiculation in all experiments, in contrast to the high degrees of supersaturation typically necessary to trigger homogeneous nucleation in rhyolites (Mangan and Sisson, 2000; Mourtada-Bonnefoi and Laporte, 2004) or phonolites (Iacono Marziano et al., 2007). The low pressure drop required to generate bubbles reflects heterogeneous nucleation, as pre-existing microlites provide surfaces for bubble embryos to form on (Hurwitz and Navon, 1994; Navon and Lyakhovsky, 1998; Gardner et al., 1999; Mangan and Sisson, 2000, Cluzel et al., 2008). Larsen (2008) reached a similar conclusion for K-phonolites at higher temperatures, and like Hurwitz and Navon (1994), suggested microscopic crystalline phases as potential nucleation sites.

In our experiments, bubbles nucleate both on and away from microlites (e.g. Fig. 5d, e, f); furthermore, as seen in other experiments, only oxides serve as bubble nucleation sites (Fig. 5e; Hurwitz and Navon, 1994; Navon and Lyakhovsky, 1998; Cluzel et al., 2008). To investigate the relationship between vesicles and microlites in more detail, oxide number densities N_{Vox} were measured in experimental series. In series A, B, and C, resulting N_{Vox} are 1×10^7, 5×10^7, and 3×10^6 respectively, 5 to 10 times higher than their corresponding vesicle number density (Table 2, Fig. 7). Thus, for each series, there are more available nucleation sites than there are nucleating bubbles. Series A and B used slightly different compositions but identical experimental procedures. Series B and C used identical starting compositions but different pre-decompression treatment (series C samples were annealed at high temperature). From this we infer that nucleation is limited by properties of the melt (water diffusivity and/or surface tension) and the time scale of decompression. As oxides are already present in the melt before decompression, oxide number density should be controlled by pre-eruptive composition and temperature rather than decompression rate. Differences in measured vesicle number density between the three series (cf. Fig. 7) are thus only partially related to the number density of oxide phases since all available nucleation sites are not utilized.

6.3. Equilibrium exsolution

To verify whether our experiments followed equilibrium exsolution paths, vesicularities measured in series A, B, and C are shown in Fig. 8 along with equilibrium curves given by Gardner et al. (1999) as:

$$\Phi = \left[\frac{\frac{\rho}{Z} \overline{V}_{H_2O} (w_I - w_F)}{1 + \left(\frac{\rho}{Z} \overline{V}_{H_2O} (w_I - w_F) \right)} \right] \quad (2)$$

where ρ is magma density in kg m^{-3}, Z is molecular water weight in kg, w_I and w_F are the weight fractions of dissolved water at initial and final pressures determined using the solubility model of Larsen (2008), and $\overline{V}_{H_2O}$ the molar volume of water (in vapor phase) at the final pressure in m^3.

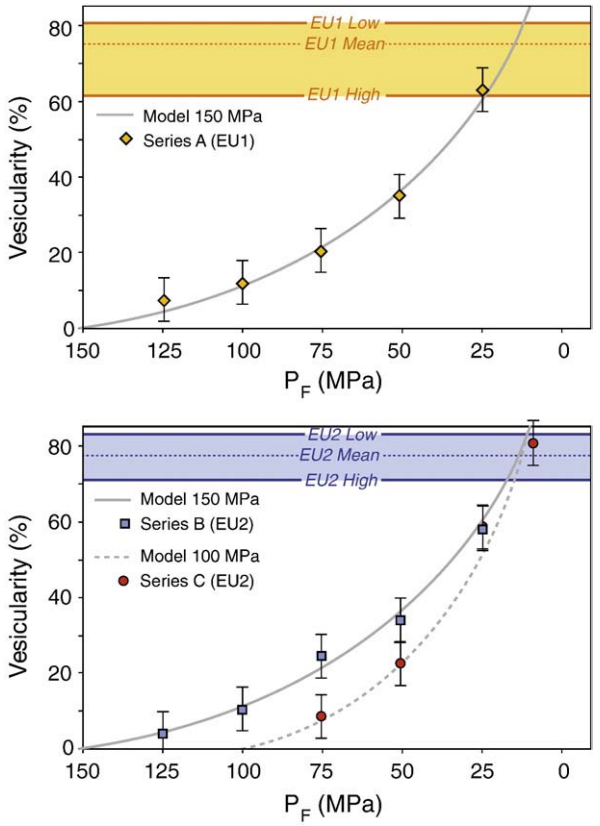

Fig. 8. Variations in vesicularity shown by experimental samples from series A, B and C compared to predicted equilibrium vesicularities following the model of Gardner et al. (1999). Vesicularities within low, mean and high density natural clasts are also reported on the *y*-axis for comparison. Maximum uncertainties reported are associated with vesicularity correction scheme imposed (see Appendix A for details).

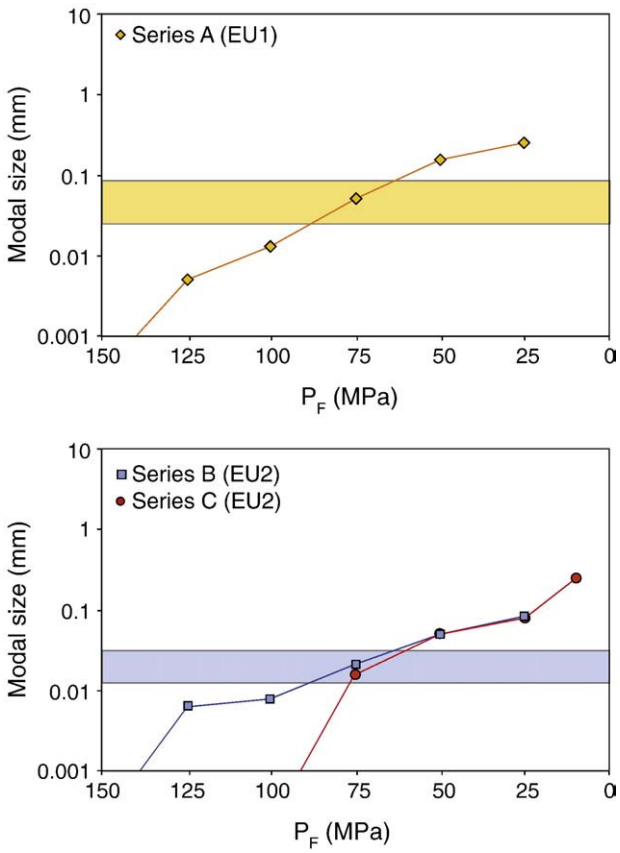

Fig. 9. Modal sizes of experimental samples obtained from size distributions from all three series. Ranges of modal sizes measured in natural samples (low, mean and high densities) are also plotted on the *y*-axis for comparison. Experimental samples all reach modal sizes measured in natural pumice at $P_F = 75$ MPa.

Within uncertainty, experimental porosities follow the equilibrium line very closely for all series, attaining about 60% at $P_F = 25$ MPa, and 82% at $P_F = 10$ MPa in series C. Thus, the experiments not only nucleated bubbles rapidly at low ΔP, but maintained equilibrium degassing paths during decompression. When compared with Larsen's (2008) results, which show disequilibrium degassing at $T = 900$ °C and decompression rates ≥ 3 MPa/s, this illustrates the sensitivity of degassing trends to both magma properties and decompression conditions (see also Larsen and Gardner, 2004).

6.4. Evolution of vesicle size during decompression

To investigate bubble growth, we compare vesicle sizes measured within experiments to those found in natural pumice. We compare modal sizes for samples representative of each final pressure achieved in series A, B and C with the ranges measured within EU1 and EU2 low, mean and high densities (Fig. 9). All series reach modal sizes measured in natural samples by $P_F \approx 75$ MPa regardless of starting pressure, which indicates that pressure exerts the primary control on bubble size. However, quenching at this pressure is unrealistic for the Vesuvius eruption. For this reason, we infer that at least one experimental variable strongly differs from 79AD eruption conditions. The most likely is decompression rate, as more rapid magma ascent and decompression implies less time spent within the conduit and smaller bubbles.

6.5. Evolution of nucleation and growth through decompression

Modal growth rate (G_{mode}) variations during decompression can be calculated directly at each 25 MPa step using modal sizes and experimental times. We consider only additional growth at each step of decompression (Table 2 and Fig. 10a). Although series A shows higher growth rates than series B, both have growth rates that increase slowly until $P_F = 90$–100 MPa, after which values increase abruptly to achieve maximum values at $P_F = 50$ MPa. Series C have maximum growth rates at lower P_F with growth rates escalating at $P_F = 25$ MPa, most likely due to the onset of coalescence.

Nucleation rates were calculated using differences in N_{Vcorr} between successive experiments divided by the decompression time interval. We compare them to those derived from classical nucleation theory (CNT). Nucleation rates depend directly on the free energy change required to form a cluster and are expressed as (Turnbull and Fisher, 1949; Hurwitz and Navon, 1994; Mangan and Sisson, 2000, 2005; Mourtada-Bonnefoi and Laporte, 2002, 2004; Cluzel et al., 2008):

$$J = J_0 \times e^{-\frac{16\pi\sigma_{hom}^3}{3kT(P_V - P_M)^2}} \quad (3)$$

where J and J_0 are nucleation rate and a pre-exponential parameter in $m^{-3}\,s^{-1}$, σ_{hom} is melt-bubble surface tension for homogeneous nucleation in $N\,m^{-1}$, k is the Boltzmann constant in $J\,K^{-1}$, T is temperature in K, and P_V and P_M are critical nucleus and melt pressures respectively.

In turn, J_0 is expressed as:

$$J_0 = \frac{2\Omega_M n_0^2 D}{a_0}\sqrt{\frac{\sigma}{kT}} \quad (4)$$

where Ω_M is volume of water molecules in the melt in m^3, D is water diffusivity in $m^2\,s^{-1}$, n_0 is the number of water molecules per unit

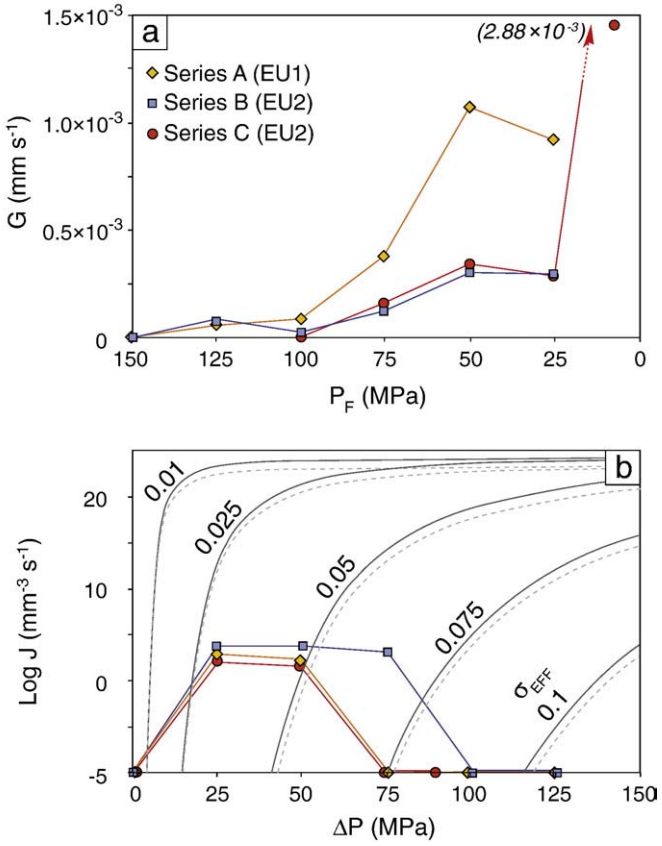

Fig. 10. (a) Growth rates G measured within experimental samples. Because G_{mode} strongly depends on final pressure rather than ΔP, growth rates are plotted against P_F. (b) Nucleation rates J are a direct function of ΔP, and values measured in experiments are compared to curves obtained from the classical nucleation theory (gray curves) for various values of effective surface tension σ_{EFF} (N m^{-1}) and a diffusivity $D = 10^{-12}$ m s^{-2}. Similar curves calculated using diffusivity values $D = 10^{-11}$ m s^{-2} are also shown for comparison (dotted lines). Exsolution in series A and B is first dominated by bubble nucleation and then subject to prevailing growth as no new bubbles are formed. In series C, growth is more influential at the onset of vesiculation. Notice that nucleation occurs through a wide range of effective surface tension values as samples are decompressed.

volume of melt in m^{-3} calculated as $n_0 = \Pi_A X_M \frac{\rho}{m}$, with Π_A being Avogadro's number, ρ the melt density in kg m^{-3}, X_M the mass fraction of water within the melt, and m the molar mass of water; finally, $a_0 \approx n_0^{-\frac{1}{3}}$ is the mean distance between neighboring water molecules (Cluzel et al., 2008). In heterogeneous nucleation, the activation energy is reduced by a factor φ expressed as (Hurwitz and Navon, 1994; Navon and Lyakhovsky, 1998):

$$\varphi = \frac{(2-\cos\theta)(1+\cos\theta)^2}{4} \quad (5)$$

where θ is the wetting angle between bubble and crystal. Because we do not know θ for the oxides that serve as nucleation sites, we replace σ_{HOM} by an "effective" surface tension σ_{EFF} that incorporates the activation energy reduction term expressed as $\sigma_{EFF} = \varphi^{1/3}\sigma_{HOM}$ (Cluzel et al., 2008). This term thus incorporates all parameters that facilitate nucleation (e.g. microlites). Our observation that there seems to be no barrier to nucleation supports the assumption that the number of nucleation sites is larger than the total number of vesicles and that $P_V \approx P_{SAT}$, where P_{SAT} is the saturation pressure and P_V the critical nuclei pressure. Thus, $P_{SAT} - P_M = \Delta P$ in nucleation rate calculations. Water diffusivity is assumed to be $D = 2\times10^{-12}$ m^2 s^{-1}, based on $D = 2\times10^{-10}$ m^2 s^{-1} for Vesuvius phonolites at $T = 1050$ °C (Iacono Marziano et al., 2007) and a factor of 100 correction to account for the temperature difference (Watson, 1994; Larsen, 2008).

Eq. (3) was solved for various effective surface tensions ranging from 0.01 to 0.1 N m^{-1}, and results are plotted along with experimental data (Fig. 10b). As expected, experiments indicate a low effective surface tension (<0.075 N m^{-1}) at $25 \le \Delta P \le 75$ MPa and nucleation rates drop to 0 at $\Delta P = 50$–75 MPa. Prolonged nucleation in series B experiments is indicated by the presence of small bubbles at $\Delta P = 75$ MPa (Fig. 6). In all series, nucleation rate trends traverse a range of effective surface tensions, as observed by Mangan and Sisson (2005) for dacites and rhyolites. After 25 MPa of decompression, all three series plot close to effective surface tensions as low as 0.030 N m^{-1} (Fig. 10b). Similar values of σ_{EFF} were found by Mourtada-Bonnefoi and Laporte (2004) in dacites using data from Gardner et al. (1999).

A comparison of growth and nucleation rates (Fig. 10a and b) reveals that nucleation is dominant for the first 50–75 MPa of decompression in series A and B, after which growth takes over. Thus, equilibrium vesicularities are maintained first by vigorous nucleation and then by diffusive growth with no addition of new bubbles. In series C, growth is much more rapid at the beginning of decompression. In all series, bubble numbers decrease at low pressures as smaller bubbles coalesce.

6.6. Comparisons with numerical models

We use the numerical models of Toramaru (1995, 2006) to predict vesicle number densities (N_{const}) as a function of decompression rate, diffusivity, and the surface tension between melt and bubbles (Yamada et al., 2005; Toramaru, 2006). For comparison with pumice samples, we use number densities $N_{Vcorr} \approx 3\times10^6$ mm^{-3} and $N_{Vcorr} \approx 11\times10^6$ mm^{-3} measured in EU1 and EU2 means respectively (Table 2). Similarly, experimental plateau values are used, that is, $N_{Vcorr} \approx 1\times10^6$ mm^{-3}, 6.5×10^6 mm^{-3}, and 0.3×10^6 mm^{-3} in series A, B and C respectively.

The number density predicted by Toramaru's model, here labeled N_{const} for constant number density, is written (Toramaru, 2006):

$$N_{const} = 34 X_0 \alpha_1^{-2} \alpha_2^{-\frac{1}{4}} \alpha_3^{-\frac{3}{2}} \quad (6)$$

Here X_0 is the initial water concentration at the saturation pressure, and α_1, α_2, α_3 represent dimensionless parameters (Toramaru, 1995) that are defined as:

$$\alpha_1 = \frac{16\pi\sigma_{HOM}^3}{3kTP_0^2} \quad (7)$$

$$\alpha_2 = \frac{\Omega_M P_0}{kT} \quad (8)$$

$$\alpha_3 = \frac{kTX_0DP_0}{4\sigma^2\frac{dP}{dt}} \quad (9)$$

As in earlier calculations, σ_{HOM} is replaced by σ_{EFF} to account for activation energy reduction during heterogeneous nucleation.

Fig. 11 shows the influence of both decompression rate (dP/dt) and effective surface tension (σ_{EFF}) on the maximum stable value of N_{const}. Experimental number densities agree well with the model if $\sigma_{EFF} = 0.02$, 0.035 and 0.045 N m^{-1} for series A, B and C respectively. These values are similar to effective surface tensions estimated for small ΔP experiments using Eq. (3) (Fig. 10b) and with estimates by Mourtada-Bonnefoi and Laporte (2004) and Mangan and Sisson (2005) for dacites. We also compare the numerical results with measured number densities (N_{Vcorr}; Table 2) for EU1 and EU2 samples. Assuming that experimental surface tensions of 0.035 N m^{-1} calculated from series A can be extrapolated to both EU1 and EU2, decompression rates of ~0.5 and 1.0 MPa/s could produce the N_{Vcorr} measured in EU1 and EU2 natural samples respectively. If, however,

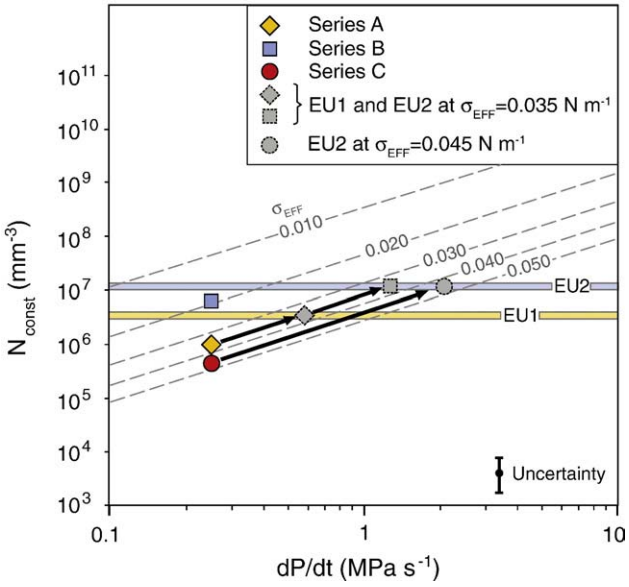

Fig. 11. Number densities per unit volume in function of ascent rate log(dP/dT) as predicted by the model of Toramaru (1995, 2006) for varying effective surface tensions σ_{EFF} = 0.01–0.05 N m^{-1} (dashed gray lines). Values measured in natural samples are also reported for comparison along with corresponding experiments (plotted according to their values of N_{Vcorr} and a dP/dt = 0.25 MPa/s). Arrows and dotted gray symbols represent the increases in dP/dT required to attain number densities measured in natural samples if a unique surface tension value of 0.035 N m^{-1} is adopted (see text for explanation). Uncertainty on N_V measured in experiments is displayed at the bottom right.

effective surface tension in EU2 was closer to series C values (i.e. 0.045 N m^{-1}), decompression rates of about 2 MPa/s are needed.

6.7. Volcanological implications

Our comparison of pumice samples, experimental charges and numerical models raises several questions. The first relates to differences in the vesiculation characteristics of EU1 and EU2 magmas. EU1 natural samples and series A experiments have larger but fewer vesicles than EU2 natural samples and series B experiments. If the differences in natural samples were solely a function of varying decompression rates, then the experiments should have yielded identical results. Shea et al. (2009) show that the compositional difference between the two eruptive units caused shifts in phase equilibria curves for leucite and other phases. Indeed, sanidine microlites crystallized vigorously within series B but not series A experiments. The textures show that the presence of sanidine affected the form, if not the rate, of vesiculation in the experiments. However EU2 pumice clasts show no evidence of sanidine. Thus, the experimental conditions chosen for replication EU2 vesiculation failed to adequately reproduce natural conditions. The recent results of Shea et al. (2009) suggest that higher experimental temperatures are necessary to prevent sanidine crystallization.

A second question relates to the observed form of the vesicle size distributions. Vesicle number densities measured within experimental samples are only slightly lower than those found in pumice. Our calculations show that decompression rates two to eight times faster would better replicate observed number densities. It follows that two hypotheses can be put forward to explain differences in number densities between the opening and the Plinian phase of the 79AD eruption: either EU1 and EU2 melts, although chemically related, are different enough that their physical properties (particularly microlite concentrations) promote bubble nucleation in EU2 magma, or EU2 erupted more rapidly than EU1. Whereas experiments suggest that the presence of oxides could significantly influence the outcome of vesiculation, field evidence supports differences in ascent rates between eruption of EU1 and EU2. Calculations of column height and discharge rate for the eruption (Carey and Sigurdsson, 1987) demonstrated that the column height increased along with discharge rate during eruption of the white magma (c.f. Fig. 1). Hence, it is likely that ascent rates within the conduit were higher during emission of EU2 than they were during the opening phase EU1.

Vesicle size variability is much broader in nature when compared to experiments (cf. Figs. 3 and 5). This variability can be quantified by comparing VVDs (Fig. 6). Additionally, it appears that modal sizes measured in EU1 and EU2 are attained too early in the inferred (experimental) decompression history (Fig. 9). This is a strong indication that vesiculation undergone by natural magmas is more complex than in simple decompression experiments. Pumice shows near-Apollonian packing configuration predicted for continuous nucleation (Blower et al., 2001, 2002), with VSDs that follow power-law distributions (exponents d = 3.4–3.6 Table 2). In contrast, experimental samples show thinner glass walls and VSDs that follow exponential distributions, indicating one or few pulses of nucleation (Blower et al., 2002). Experiments show that nucleation is not steady for a constant decompression rate (Fig. 10b) but rather peaks and drops fairly rapidly. Hence, the pressure perturbation responsible for continuous nucleation during ascent of natural magmas is unlikely to be generated by a steady decompression rate, as in the experiments. This confirms that magmas such as those involved in the 79AD eruption have more complex ascent and vesiculation histories than simple "continuous nucleation and growth" models often proposed to account for vesicle textures observed in pyroclasts.

6.8. Comparisons with other magmas and implications for the style of ascent

Larsen's (2008) experiments run at EU2 temperatures (T = 900 °C) and dP/dT ≥ 3 MPa/s, did not show equilibrium degassing. Experiments on rhyolitic magmas show similar disequilibrium at decompression rates >0.025 MPa/s, due to much slower diffusion and resulting build-up of high supersaturation levels (Gardner et al., 1999; Mangan and Sisson, 2000; Mourtada-Bonnefoi and Laporte, 2004; Cluzel et al., 2008). A common conclusion is that impeded nucleation may be the key to generating the extreme explosivity of silicic magmas. In most models, because diffusion is slow in rhyolites or rhyodacites, bubbles nucleate in numbers reaching 10^6–10^7 mm^{-3} (Mourtada-Bonnefoi and Laporte, 1999, 2002; Gardner and Denis, 2004) only after the critical supersaturation pressure is exceeded. In microlite-bearing K-phonolites, no supersaturation is needed for bubbles to nucleate; nevertheless they attain numbers similar to those measured in more silicic magmas (Larsen and Gardner, 2004; Iacono Marziano et al., 2007; Larsen, 2008; this study).

The difference in vesiculation behavior between more evolved silicic and less evolved alkalic magmas has important implications for the style of volcanic eruption. If rhyolitic melts are brought to extremely unstable thermodynamic states by build-up of oversaturation, they may fragment as a consequence of sudden nucleation and growth (e.g. Cluzel et al., 2008). In contrast, phonolitic melts tend to track equilibrium water contents and vesicularities along the decompression path, as long as ascent rates are lower than 5 MPa/s. It is thus much more likely that fast ascent is the main fragmentation-triggering mechanism in phonolite systems, ultimately responsible for initiating and sustaining the Plinian eruption of Vesuvius in 79AD.

6.9. The uses and limits of linear laboratory vesiculation experiments

We have illustrated how textures observed in experimental runs are a subtle balance between nucleation and diffusive growth of bubbles. When abundant nucleation sites are available (series A and B) nucleation dominates, and as the space between bubbles is reduced, diffusive growth becomes dominant (Fig. 10). However, as mentioned

previously, this behavior (i.e. one pulse of nucleation and growth) occurs only in systems undergoing linear, constant decompressions through time. While this condition may be satisfied for certain phases of magmatic ascent, studies have shown that magma likely ascends in a non-linear fashion, entering the conduit rather slowly and accelerating until the fragmentation level (e.g. Neri et al., 2002). In this model, primary nucleation events form fewer large bubbles when decompression rates are slow enough, and countless smaller bubbles form following secondary nucleation events towards the upper regions of the conduit due to substantial acceleration (Mourtada-Bonnefoi and Laporte, 2004; Massol and Koyaguchi, 2005; Cluzel et al., 2008). This non-linearity is thought to be responsible for the bi-modality of vesicle size distributions often measured in natural pumice (Cluzel et al., 2008). In 79AD white pumice VSDs, bi-modality is not ubiquitous (Fig. 4). High density clasts for both EU1 and EU2 do not record a clear bi-modal distribution and the second mode observed in EU1 and EU2 low density clasts as well as the EU2 mean density population may result from coalescence or could have formed deeper in the conduit. Assuming that bubbles do not have time to entirely decouple from the melt, the superimposition of size ranges resulting from each nucleation events could then generate the wide and complex size distributions typically measured in natural pumice. It is difficult to assess in detail the effects of non-linear ascent rates on textures at the laboratory scale, and such experiments have not been yet attempted. In the future, non-linear vesiculation experiments involving either numerous pressure drops with decreasing hold times or involving continuously increasing decompression rates need to be tested in order to evaluate the influence of variations during the decompression path on resulting vesicle textures.

7. Conclusions

Experiments involving decompression of K-phonolites were compared to natural samples erupted during the opening and plinian phases of the 79AD eruption of Vesuvius. At conditions initially inferred for ascent of the Vesuvius 79AD white magma (100 MPa$<P_f<$ 150 MPa, $T=850$ °C, $dP/dT=0.25$ MPa/s), experimental samples produce vesicle number densities within the same order of magnitude of those measured in EU1 and EU2 pumices, and bubbles of equivalent sizes at final pressures unrealistically high for the natural environment. Experiments exsolve their water in equilibrium with the melt at the applied decompression rates; however, vesicle size distributions are somewhat different from those shown by natural EU1 and EU2 samples. Number densities rapidly reach their maximum and stabilize (around 10^6 and 10^7 mm^{-3} in EU1 and EU2 respectively), as predicted by Toramaru (2006), and low effective surface tensions ($\sigma_{EFF}\sim0.035$ N m^{-1}) are needed to generate such high values at ascent rate conditions suggested for the 79AD eruption. In nature and within the experiments, EU1 shows fewer but larger vesicles than EU2; this can be related both to small differences in ascent rates (EU2 faster than EU1) and compositional differences within the melts (i.e. influence of microlites).

From this study, we infer that the wide and often polymodal size distributions measured in natural samples can be obtained if magma endures non-linear pressure perturbations and if nucleation pulses are triggered at various levels in the conduit. In this model, modal sizes observed in EU1 and EU2 samples result from bubble growth in the upper part of the conduit as ascent accelerates, as opposed to being generated throughout decompression. In turn, experiments show that the high number densities measured in natural samples can be reached as long as decompression rates of the order of 0.5–1 MPa/s are attained during ascent.

Finally, comparisons made between K-phonolites and more evolved silicic magmas such as rhyolites illustrate how diverging ascent histories may both result in similar catastrophic plinian eruptions. Through detailed investigations of natural pumice and laboratory vesicular samples, therefore, significant progress is being made towards understanding how complex textures observed at the surface may form. Future experiments should perhaps include the possibility of exploring non-linear decompression rates in the laboratory in order to even better replicate natural pumice textures.

Acknowledgments

The authors wish to acknowledge the NSF grants EAR 0537950, 0537543, and 0511070 (J. Larsen). We thank Clara Margalef and Leslie Almberg for help in the lab. Thomas Giachetti, Tim Druitt, Nicolas Cluzel, Didier Laporte, Carrie Brugger, Owen Neill and Lisa Petrochilos are thanked for the helpful discussions. Reviews and suggestions by Alain Burgisser and Jacopo Taddeucci considerably improved the quality of this manuscript.

Appendix A

In an attempt to estimate how 2D (i.e. "image vesicularity",ϕ_{2D}) compares to true vesicularity ("density-derived vesicularity",ϕ_{3D}), we gathered data from 5 explosive and 1 effusive eruptions including Mt. St Helens (Washington, USA) (Klug and Cashman, 1994), Vesuvius (Naples, Italy) 79AD white and gray pumice (Gurioli et al., 2005), 1912AD Novarupta (Alaska, USA) (Adams et al., 2006), Makapu'u lava flows (Hawaii, USA, Gurioli, unpublished data), Kilauea Iki (Hawaii, Stovall et al., in prep.), and Villarica (Chile) (Gurioli et al., 2008). To provide a useful value applicable to experiments, 2D vesicularity was measured at the highest image magnification used for each individual study. This means that much like in the experiments, large bubbles are often discarded and image vesicularity tends to be lower than true vesicularity. Indeed, Fig. A1 shows that while "image" and "true" vesicularities compare well at very high values (i.e. >70–75%), image vesicularity tends to underestimate the true vesicularity at lower values. The fitted 2nd degree polynomial curve is given in the main text (Eq. (1)).

While the fit is fairly good ($R^2=0.85$), a typical spread of about ±5–10% (mean error = 4.3% with $1\sigma=3.08$) is to be expected if the relationship is to be used to derive "true" 3D vesicularities from 2D image fraction area measurements. These uncertainties most likely originate from the frequent non-sphericity of vesicles in volcanic pyroclasts, and, more importantly, from the lower probability of encountering smaller objects when performing cross-sections within samples (Sahagian and Proussevitch, 1998). Although difficult to quantify due to the lack of data at $\phi_{3D}<30\%$ in Fig. A1, uncertainties will inherently be much larger for samples with low vesicularities (i.e.

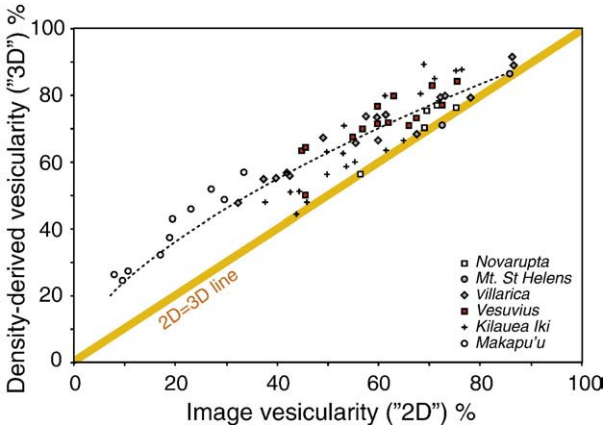

Fig. A1. Comparisons between vesicularities measured in thin sections (ϕ_{2D}) with those derived from density measurements (ϕ_{3D}). Note how the data fails to track the orange-colored 1:1 line.

less probability of encountering fewer large vesicles or numerous very small ones), than for high vesicularity ones. Hence, even if it is far from perfect, extrapolation of vesicularities using Eq. (1) provides a better alternative than simply reporting 2D measurements of vesicle area within experimental samples.

References

Adams, N.K., Houghton, B.F., Fagents, S.A., Hildreth, W., 2006. The transition from explosive to effusive eruptive regime: the example of the 1912 Novarupta eruption, Alaska. Geol. Soc. Am. Bull. 118, 620–634. doi:10.1130/B25768.1.

Bai, L., Baker, D., Rivers, M., 2008. Experimental study of bubble growth in Stromboli basalt melts at 1 atm. Earth Planet. Sci. Lett. 267, 533–547.

Barberi, F., Bizouard, B., Clocchiatti, R., Metrich, N., Santacroce, R., Sbrana, A., 1981. The Somma-Vesuvius chamber: a petrological and volcanological approach. Bull. Volcanol. 44, 295–315.

Blower, J.D., Keating, J.P., Mader, H.M., Phillips, J.C., 2001. Inferring volcanic degassing processes from vesicle size distributions. Geophys. Res. Lett. 28, 347–350. doi:10.1029/2000GL012188.

Blower, J.D., Keating, J.P., Mader, H.M., Phillips, J.C., 2002. The evolution of bubble size distributions in volcanic eruptions. J. Volcanol. Geotherm. Res. 120, 1–23.

Burgisser, A., Gardner, J.E., 2005. Experimental constraints on degassing and permeability in volcanic conduit flow. Bull. Volcanol. 67, 42–56.

Carey, S., Sigurdsson, H., 1987. Temporal variations in column height and magma discharge rate during the 79 A.D. eruption of Vesuvius. Geol. Soc. Am. Bull. 99, 303–314.

Cashman, K.V., Mangan, M.T., 1994. Physical Aspects of Magmatic Degassing II: Constraints on Vesiculation Processes from Textural Studies of Eruptive Products. In: Carroll, M. (Ed.), Volatiles in Magmas. Min. Soc. Am, Washington, D.C, pp. 447–478.

Cashman, K.V., Marsh, B.D., 1988. Crystal size distribution (CSD) in rocks and the kinetics and dynamics of crystallisation II. Makaopuhi lava lake. Contrib. Mineral. Petrol. 99, 292–305.

Cioni, R., 2000. Volatile content and degassing processes in the 79AD magma chamber at Vesuvius (Italy). Contrib. Mineral. Petrol. 140, 40–54.

Cioni, R., Marianelli, P., Sbrana, A., 1992. Dynamics of the AD 79 eruption: stratigraphic, sedimentological and geochemical data on the successions from the Somma-Vesuvius southern and eastern sectors. Acta Vulcanol. 2, 109–123.

Cioni, R., Civetta, L., Marianelli, P., Metrich, N., Santacroce, R., Sbrana, A., 1995. Compositional layering and syn-eruptive mixing of periodically refilled shallow magma chamber: the A.D. 79 Plinian eruption of Vesuvius. J. Pet. 36, 739–776.

Cioni, R., Marianelli, P., Santacroce, R., 1998. Thermal and compositional evolution of the shallow magma chamber of Vesuvius: evidence from pyroxene phenocrysts and melt inclusions. J. Geophys. Res. 103 (B8), 18277–18294.

Cioni, R., Gurioli, L., Sbrana, A., Vougioukalakis, G., 2000. Precursors to the Plinian eruptions of thera (late bronze age) and Vesuvius (AD 79): data from archaeological areas. J. Volcanol. Geoth. Res. 177, 719–724.

Cioni, R., Bertagnini, A., Santacroce, R., Andronico, D., 2008. Explosive activity and eruption scenarios at Somma-Vesuvius (Italy): Towards a new classification scheme. J. Volcanol. Geotherm. Res. 178, 331–346.

Cluzel, N., Laporte, D., Provost, A., Kannewischer, I., 2008. Kinetics of heterogeneous bubble nucleation in rhyolitic melts: implications for the number density of bubbles in volcanic conduits and for pumice textures. Contrib. Mineral. Petrol. 156, 745–763.

Gardner, J.E., 2007. Heterogeneous bubble nucleation in highly viscous silicate melts during instantaneous decompression from high pressure. Chem. Geol. 236, 1–12. doi:10.1016/j.chemgeo.2006.08.006.

Gardner, J.E., Denis, M.-H., 2004. Heterogeneous bubble nucleation on Fe–Ti oxide crystals in high-silica rhyolitic melts. Geochim. Cosmochim. Acta 68, 3587–3597.

Gardner, J.E., Hilton, M., Carroll, M.R., 1999. Experimental constraints on degassing of magma: isothermal bubble growth during continuous decompression from high pressure. Earth Planet. Sci. Lett. 168, 201–218.

Gardner, J.E., Hilton, M., Carroll, M.R., 2000. Bubble growth in highly viscous silicate melts during continuous decompression fromhigh pressure. Geochim. Cosmochim. Acta 64, 1473–1483.

Gonnermann, H.M., Manga, M., 2007. The fluids mechanics of volcanic eruptions. Ann. Rev. Fluid Mech. 39, 321–356.

Gurioli, L., Houghton, B.F., Cashman, K.V., Cioni, R., 2005. Complex changes in eruption dynamics during the 79AD eruption of Vesuvius. Bull. Volcanol. 67, 144–159.

Gurioli, L., Harris, A.J.L., Houghton, B.F., Polacci, M., Ripepe, M., 2008. Textural and geophysical characterization of explosive basaltic activity at Villarrica volcano. J. Geophys. Res. 113, B08206. doi:10.1029/2007JB005328.

Houghton, B.F., Wilson, C.J.N., 1989. A vesicularity index for pyroclastic deposits. Bull. Volcanol. 51, 451–462.

Hurwitz, S., Navon, O., 1994. Bubble nucleation in rhyolitic melts: experiments at high pressure, temperature, and water content. Earth Planet. Sci. Lett. 122, 267–280.

Iacono Marziano, G., Schmidt, B.C., Dolfi, D., 2007. Equilibrium and disequilibrium degassing of a phonolitic melt (Vesuvius AD 79 "white pumice") simulated by decompression experiments. J. Volcanol. Geotherm. Res. 161, 151–164.

Jaupart, C., 1996. Physical models of volcanic eruptions. Chem. Geol. 128, 217–227. doi:10.1016/0009-2541(95)00175-1.

Klug, C., Cashman, K.V., 1994. Vesiculation of May 18, 1980, Mount St. Helens magma. Geology 22, 468–472.

Klug, C., Cashman, K.V., Bacon, C., 2002. Structure and physical characteristics of pumice from the climactic eruption of Mount Mazama (Crater Lake), Oregon. Bull. Volcanol. 64, 486–501.

Larsen, J.F., 2008. Heterogeneous bubble nucleation and disequilibrium H2O exsolution in Vesuvius K-phonolite melts. J. Volcanol. Geotherm. Res. 275, 278–288.

Larsen, J.F., Gardner, J.E., 2000. Experimental constraints on bubble interactions in rhyolite melts: implications for vesicle size distributions. Earth Planet. Sci. Lett. 180, 201–214.

Larsen, J.F., Gardner, J.E., 2004. Experimental study of water degassing from phonolite melts: implications for volatile oversaturation during magmatic ascent. J. Volcanol. Geotherm. Res. 134, 109–124.

Larsen, J.F., Denis, M.-H., Gardner, J.E., 2004. Experimental study of bubble coalescence in rhyolitic and phonolitic melts. Geochim. Cosmochim. Acta 68, 333–344.

Lautze, N.C., Houghton, B.F., 2007. Linking variable explosion style and magma textures during 2002 at Stromboli volcano, Italy. Bull. Volcanol. 69, 445–460.

Lensky, N.G., Navon, O., Lyakhovsky, V., 2004. Bubble growth during decompression of magma: experimental and theoretical investigation. J. Volcanol. Geotherm. Res. 129, 7–22.

Lirer, L., Pescatore, T., Booth, B., Walker, G.P.L., 1973. Two plinian pumice-fall deposits from Somma-Vesuvius Italy. Geol. Soc. Am. Bull. 84, 759–772.

Lovejoy, S., Gaonac'h, H., Schertzer, D., 2004. Bubble distributions and dynamics: the expansion–coalescence equation. J. Geophys. Res. 109, B11203. doi:10.1029/2003JB002823.

Lyakhovsky, V., Hurwitz, S., Navon, O., 1996. Bubble growth in rhyolitic melts: experimental and numerical investigation. Bull. Volcanol. 58, 19–32.

Mangan, M.T., Cashman, K.V., 1996. The structure of basaltic scoria and reticulite and inferences for vesiculation, foam formation, and fragmentation in lava fountains. J. Volcanol. Geotherm. Res. 73, 1–18.

Mangan, M., Sisson, T., 2000. Delayed, disequilibrium degassing in rhyolite magma: decompression experiments and implications for explosive volcanism. Earth Planet. Sci. Lett. 183, 441–455.

Mangan, M.T., Sisson, T.W., 2005. Evolution of melt-vapor surface tension in silicic volcanic systems: experiments with hydrous melts. J. Geophys. Res. 110, B01202.

Mangan, M.T., Sisson, T.W., Hankins, W.B., 2004. Decompression experiments identify kinetic controls on explosive silicic eruptions. Geophys. Res. Lett. 31, L08605.

Martel, C., Schmidt, B.C., 2003. Decompression experiments as an insight into ascent rates of silicic magmas. Contrib. Mineral. Petrol. 144, 397–415.

Massol, H., Koyaguchi, T., 2005. The effect of magma flow on nucleation of gas bubbles in a volcanic conduit. J. Volcanol. Geotherm. Res. 143, 69–88.

Mastin, L.G., Ghiorso, M.S., 2000. A Numerical Program for Steady-State Flow of Magma–Gas Mixtures Through Vertical Eruptive Conduits. USGS Open-File Report, 00-209.

Mongrain, J., Larsen, J.F., King, P.L., 2008. Rapid water exsolution, degassing, and bubble collapse observed experimentally in K-phonolite melts. J. Volcanol. Geoth. Res. 173, 178–184.

Mourtada-Bonnefoi, C.C., Laporte, D., 1999. Experimental study of homogeneous bubble nucleation in rhyolitic magmas. Geophys. Res. Lett. 26, 3505–3508.

Mourtada-Bonnefoi, C.C., Laporte, D., 2002. Homogeneous bubble nucleation in rhyoliticmagmas: an experimental study of the effect of H_2O and CO_2. J. Geophys. Res. 107, B4. doi:10.1029/2001JB00290.

Mourtada-Bonnefoi, C.C., Laporte, D., 2004. Kinetics of bubble nucleation in a rhyolitic melt: an experimental study of the effect of ascent rate. Earth Planet. Sci. Lett. 218, 521–537.

Navon, O., Lyakhovsky, V., 1998. Vesiculation Processes in Silicic Magmas. In: Gilbert, J.S., Sparks, R.S.J. (Eds.), The Physics of Explosive Volcanic Eruptions: Geol. Soc. Lond. Spec. Pub., vol. 145, pp. 27–50.

Neri, A., Papale, P., Del Seppia, D., Santacroce, R., 2002. Coupled conduit and atmospheric dispersal dynamics of the AD 79 Plinian eruption of Vesuvius. J. Volcanol. Geoth. Res. 120, 141–160.

Papale, P., Dobran, F., 1993. Modeling of the ascent of magma during the Plinian eruption of Vesuvius in A.D. 79. J. Volcanol. Geoth. Res. 58, 101–132.

Polacci, M., Papale, P., Rosi, M., 2001. Textural heterogeneities in pumices from the climactic eruption of Mount Pinatubo, 15 June 1991, and implication for magma ascent dynamics. Bull. Volcanol. 63, 83–97.

Polacci, M., Pioli, L., Rosi, M., 2003. The plinian phase of the Campanian Ignimbrite eruption (Phlegrean Fields, Italy): evidence from density measurements and textural characterization of pumice. Bull. Volcanol. 65, 418–432. doi:10.1007/s00445-002-0268-4.

Polacci, M., Baker, D.R., Bai, L., Mancini, L., 2007. Large vesicles record pathways of degassing at basaltic volcanoes. Bull. Volcanol. 70, 1023–1029. doi:10.1007/s00445-007-0184-8.

Rolandi, G., Paone, A., Di Lascio, M., Stefani, G., 2008. The 79AD eruption of Somma: the relationship between the date of the eruption and the southeast tephra dispersion. J. Volcanol. Geoth. Res. 169, 87–98.

Rutherford, M.J., 1996. Conditions in the Pre-eruption 79AD Vesuvius Magmas: Controls on Magmatic and Eruption Processes. Vesuvius Decade Volcano, Workshop Handbook, IAVCEI-CEV, IAVCEI-CMVD, 17–22 September 1996.

Sable, J.E., Houghton, B.F., Wilson, C.J.N., Carey, R.J., 2006. Complex proximal sedimentation from Plinian plumes: the example of Tarawera 1886. Bull. Volcanol. 69, 89–103.

Sahagian, D.L., Proussevitch, A.A., 1998. 3D particle size distributions from 2D observations: stereology for natural applications. J. Volcanol. Geoth. Res. 84, 173–196.

Scaillet, B., Pichavant, M., 2004. Crystallization conditions of Vesuvius phonolites. Geophys. Res. Abstr. 6, 03764.

Scaillet, B., Pichavant, M., Cioni, R., 2008. Upward migration of Vesuvius magma chamber over the past 20, 000 years. Nature 455, 216–220.

Shea, T., Larsen, J.F., Gurioli, L., Hammer, J.E., Houghton, B.F., Cioni, R., 2009. Leucite crystals: surviving witnesses of magmatic processes preceding the 79AD eruption at Vesuvius, Italy. Earth Planet. Sci. Lett. 281, 88–98. doi:10.1016/j.epsl.2009.02.014.

Shea, T., Houghton, B.F., Gurioli, L., Cashman, K.V., Hammer, J.E., Hobden, B., 2010. Textural studies of vesicles in volcanic rocks: an integrated methodology. J. Volcanol. Geotherm. Res. 190, 271–289. doi:10.1016/j.jvolgeores.2009.12.003.
Sigurdsson, H., Cashdollar, S., Sparks, R.S.J., 1982. The eruption of Vesuvius in AD 79: reconstruction from historical and volcanological evidence. Am. J. Archaeo. 86, 39–51.
Sigurdsson, H., Carey, S., Cornell, W., Pescatore, T., 1985. The Eruption of Vesuvius in A.D. 79. Nat. Geog. Res. 1, 332–387.
Sigurdsson, H., Cornell, W., Carey, S., 1990. Influence of magma withdrawal on compositional gradients during the AD 79 Vesuvius eruption. Nature 345, 519–521.
Suzuki, Y., Gardner, J.E., Larsen, J.F., 2007. Experimental constraints on syneruptive magma ascent related to the phreatomagmatic phase of the 2000AD eruption of Usu volcano, Japan. Bull. Volcanol. 69, 423–444.
Toramaru, A., 1989. Vesiculation process and bubble size distributions in ascending magmas with constant velocities. J. Geophys. Res. 94 (B12), 17523–17542.
Toramaru, A., 1995. Numerical study of nucleation and growth of bubbles in viscous magmas. J. Geophys. Res. 100, 1913–1931.
Toramaru, A., 2006. BND (bubble number density) decompression rate meter for explosive volcanic eruptions. J. Volcanol. Geoth. Res. 154, 303–316.
Turnbull, D., Fisher, J.C., 1949. Rates of nucleation in condensed systems. J. Chem. Phys. 17, 71–73.
Vergniolle, S., 1996. Bubble size distribution in magma chambers and dynamics of basaltic eruptions. Earth Planet. Sci. Lett. 140, 269–279.
Watson, E.B., 1994. Diffusion in volatile-bearing magmas. Rev. Mineral. 30, 371–411.
Yamada, K., Tanaka, H., Nakazawa, K., Emori, H., 2005. A new theory of bubble formation in magma. J. Geophys. Res. 110, B02203.